Decorrelation rate and daily cycle in sub-daily time series of SAR coherence amplitude

Villarroya-Carpio, Arturo; Lopez-Sanchez, Juan M.; Aguasca, Albert; Mas, Mireia; Fàbregas, Xavier; Broquetas, Antoni; Steele-Dunne, Susan C.

DOI
10.1016/j.rse.2024.114358

Publication date
2024

Document Version
Final published version

Published in
Remote Sensing of Environment

Citation (APA)
Villarroya-Carpio, A., Lopez-Sanchez, J. M., Aguasca, A., Mas, M., Fàbregas, X., Broquetas, A., & Steele-Dunne, S. C. (2024). Decorrelation rate and daily cycle in sub-daily time series of SAR coherence amplitude. *Remote Sensing of Environment*, *313*, Article 114358. https://doi.org/10.1016/j.rse.2024.114358

Remote Sensing of Environment 313 (2024) 114358

Contents lists available at ScienceDirect

Remote Sensing of Environment

journal homepage: www.elsevier.com/locate/rse

Decorrelation rate and daily cycle in sub-daily time series of SAR coherence amplitude

Arturo Villarroya-Carpio [a], Juan M. Lopez-Sanchez [a,*], Albert Aguasca [b], Mireia Mas [b], Xavier Fàbregas [b], Antoni Broquetas [b], Susan C. Steele-Dunne [c]

[a] Institute for Computer Research, University of Alicante, Alicante, Spain
[b] CommSensLab, Dept. Signal Theory and Communications, Univ. Politècnica de Catalunya, Barcelona, Spain
[c] Dept. Geosciences and Remote Sensing, Fac. Civil Eng. and Geosciences, TU Delft, Delft, The Netherlands

ARTICLE INFO

Edited by Jing M. Chen

Keywords:
Agriculture
Synthetic aperture radar (SAR)
Interferometric coherence
Soil moisture
Daily cycle
Vegetation
Phenology

ABSTRACT

A dataset of sub-daily C-band data, acquired with a ground-based synthetic aperture radar, has been used to study soil and vegetation dynamics during a complete growing season in a controlled agricultural test site. The data have been exploited to analyse the rate and sources of decorrelation in the scene, as well as the consequences of the observation conditions of a sub-daily satellite (with either low, medium or geosynchronous orbit): short revisit times, availability of multiple acquisitions during a single day, and shallow observations at some incidence angles. Repeat-pass coherence is found to be less affected by temporal decorrelation when the primary image is acquired during nighttime or the last hours predawn. Regarding the incidence angle, VV has increased sensitivity to certain phenological stages as the incidence angle increases. Additionally, a periodic oscillation on a sub-daily scale is observed when creating coherence time series with increasing temporal baseline. Factors which strongly contribute to these oscillations are the daily cycles of temperature, soil moisture and vegetation water dynamics.

1. Introduction

The use of Synthetic Aperture Radar (SAR) data is becoming more widespread in the field of agriculture, due to its improved spatial resolution over wide areas compared to passive microwave remote sensing and its generally better temporal coverage than optical imagery, on account of not being affected by the presence of clouds (Steele-Dunne et al., 2017). SAR data have been used in multiple crop monitoring applications, from crop type classification to estimation of biophysical parameters and crop yield, through the use of backscattering coefficients, polarimetry or interferometry (Lopez-Sanchez and Ballester-Berman, 2009; Liu et al., 2019; Mandal et al., 2021).

SAR interferometry (InSAR) provides coherence and phase measurements related to the scene's geometry and dielectric properties and their stability (Bamler and Hartl, 1998). Different factors, related to the scene, sensor characteristics, and processing, influence the interferometric coherence (Zebker and Villasenor, 1992; Touzi et al., 1999).

Repeat-pass SAR interferometry involves combining pairs of images acquired at different times and is typically employed with images from the same satellite gathered in different passes. In the context of agriculture, repeat-pass InSAR coherence has been successfully exploited for different purposes. Bare soil keeps high coherence unless the moisture content changes, whereas vegetated areas suffer from temporal decorrelation, which is also dependent on the characteristics and growth periods of the specific crop. For this reason, time series of interferometric coherence have been a useful tool for crop-type classification (Busquier et al., 2020; Mestre-Quereda et al., 2020; Nikaein et al., 2021). Series of coherence constructed from ERS data were also used for retrieval of biophysical variables, such as crop height and canopy cover (Wegmuller and Werner, 1997; Engdahl et al., 2001; Blaes and Defourny, 2003), at a time when the lack of SAR images with short revisit times was a limiting factor.

The launch of the Sentinel-1 constellation has enabled the systematic use of repeat-pass interferometry for crop monitoring. Ouaadi et al. (2020b) explored the use of Sentinel-1 backscatter and interferometric coherence for monitoring wheat, with an emphasis on the sensitivity of SAR data to vegetation water content and soil moisture (SM). In (Khabbazan et al., 2019; Nasirzadehdizaji et al., 2021; Pandit et al., 2022), time series of backscattering and coherence amplitude were used for crop monitoring and identification of the main phenological stages of

* Corresponding author.
E-mail addresses: arturo.villarroya@ua.es (A. Villarroya-Carpio), juanma.lopez@ua.es (J.M. Lopez-Sanchez).

https://doi.org/10.1016/j.rse.2024.114358
Received 3 June 2024; Received in revised form 22 July 2024; Accepted 5 August 2024
Available online 20 August 2024

various crops. In addition, Villarroya-Carpio et al. (2022) found good correlations between coherence time series and NDVI for a wide variety of crops. These observations were later confirmed over several growing seasons (Villarroya-Carpio and Lopez-Sanchez, 2023).

Besides the dependence of repeat-pass InSAR coherence on the crop calendar and vegetation properties, interferometric data are also sensitive to SM. SM is a key variable in hydrology, meteorology, and climatology applications, but it is also relevant in agriculture (Seneviratne et al., 2010), since it influences crop management and irrigation planning. Given the difficulty of measuring SM on a large scale and routinely, there has been a wide interest in the use of remote sensing techniques for SM retrieval. Thermal infrared and passive microwave imagery have been used for this purpose but their suitability in agriculture applications is limited by their coarse spatial resolution. SAR data offer an important improvement in this issue, while still facing challenges related to sparse temporal sampling, the impact of the incidence angle of the observation, sensitivity only to the first centimetres of soil (i.e. no direct information about SM at the root zone) (Mohanty et al., 2017), and the superimposed contributions of vegetation and surface scattering (Wagner et al., 1999a).

There have been multiple studies utilising SAR for SM retrieval through the use of different bands (Shi et al., 1997; Le Hegarat-Mascle et al., 2002) and techniques (Kornelsen and Coulibaly, 2013). More recently, the use Sentinel-1 has been evaluated (Bauer-Marschallinger et al., 2019; Balenzano et al., 2021; Palmisano et al., 2021). SAR interferometry in particular also carries information about SM (Morrison et al., 2011; De Zan et al., 2014). Particularly, the inversion of SM from SAR phase closure has been explored recently (De Zan et al., 2015; De Zan and Gomba, 2018; Michaelides and Zebker, 2020; Palmisano et al., 2022).

Regarding the water content of plants, detection of water stress in vegetation is another crucial point of interest in the context of crop monitoring, and it is directly linked to SM dynamics. Various techniques have been utilised to track water stress in crops, including the use of SM sensors or optical imagery (Ihuoma and Madramootoo, 2017), but also using radar data, exploiting both backscatter and coherence (van Emmerik et al., 2015; Ouaadi et al., 2020a).

In recent years there has been a growing interest in the necessity of acquiring SAR imagery at increased temporal resolution, particularly at sub-daily scales. In this line, different mission proposals have developed plans for systems providing sub-daily SAR observations. Hydroterra was a mission concept for a geosynchronous SAR satellite, proposed as a candidate for ESA's 10th Earth Explorer (ESA, 2020). The main focus of the mission was to observe and understand the details of the daily water cycle over land, with potential applications on hydrology, water management, climate research, etc. More recently, the Sub-daily Land Atmosphere INTEractions (SLAINTE) mission idea, submitted in response to the 12th call for ESA Earth Explorers, aimed to bridge the observation gap at sub-daily scales (Steele-Dunne et al., 2024). However, very few studies have examined the sensitivity of radar data to changes in the scene for these short revisit times. The ESA-funded BorealScat campaign (Monteith and Ulander, 2022) conducted a 5-year-long experiment focused on monitoring a forested area with sub-hourly C, L and P-band radar observations. This long time series allowed to identify both daily and seasonal changes in the radar response, attributed to wind-induced movement in the scatterers, evapotranspiration (ET), changes in SM, water content in the canopy, etc. A previous similar work (Hamadi et al., 2014), also part of the preliminary research in preparation for ESA's BIOMASS mission, analysed 5 months of ground-based P-band data over a tropical forest. They observed a diurnal cycle in repeat-pass coherence, and its disturbances caused by rainfall. Some studies have focused on sub-daily variations in radar backscatter over agricultural scenes (e.g. van Emmerik et al. (2015), Khabbazan et al. (2022)). In a more recent study, Ouaadi et al. (2024) carried out a ground-based experiment in order to investigate this diurnal cycle of the interferometric coherence over wheat croplands in a semi-arid region. That paper described the observed influence of irrigation, wind, SM and vegetation water content on C-band coherence time series, highlighting the potential of using this type of data for crop water status monitoring.

The present study is focused on exploiting data from the HydroSoil campaign (Aguasca et al., 2020; Mas et al., 2024), which emulated the observation conditions (shallow incidence angles, sub-daily acquisitions, etc.) of the Hydroterra mission over an agricultural area. One of the goals of the campaign was to study the dynamics of SAR interferometry at sub-daily timescales. A key point of interest is to evaluate the impact of large incidence angles (conventional SAR satellites rarely operate for angles larger than 45–50°). Only recently there has been research carried out about these observation conditions (Ouaadi et al., 2024), which could have an impact on the performance of a geosynchronous SAR.

Given the availability of multiple temporal baselines, a first objective of this research is to study the rate of decorrelation of an agricultural area at different moments during the season, as well as the effect of the incidence angle and the choice of time of acquisition during the day. Emphasis is placed on the mathematical modelling of the coherence for increasing temporal baselines in both short and long-term scenarios. Secondly, the evolution of the interferometric coherence within a day is studied, particularly its sensitivity to SM and daily dynamics of the vegetation and its water content.

2. Materials and methods

2.1. Dataset

The HydroSoil campaign (Aguasca et al., 2020; Mas et al., 2024), led by the CommSensLab Department, from the Universitat Politècnica de Catalunya, was carried out in a test site near the Barcelona School of Agri-Food and Biosystems Engineering (Fig. 1a). It provided continuous ground-based SAR monitoring of a controlled agricultural field (Fig. 1b, left) during nine months in 2020, from March through November. The radar instrument acquired single-look complex (SLC) C-band fully-polarimetric imagery with a revisit time of 10 min and notably shallow incidence angles (defining incidence angle as the angle between the radar beam direction and a line normal to the surface), varying between 55°and 70° (Fig. 1b, right).

The ground-based SAR system employed the polarimetric-radiometric calibration algorithm proposed by Sarabandi et al. (1990). This method requires high isolation between antenna ports, with a cross-polarisation isolation better than 25 dB, a condition met by the radar system. It is particularly effective for field calibration, needing only two calibrators: a perfectly co-polar target (e.g., a trihedral) with a well-known radar cross section, and a target exhibiting significant cross-polar response (e.g., a 45° rotated dihedral).

The radar system had a good inherent stability in time, which was obtained with thermal control of the circuitry. An in-depth analysis of the system's stability during the measurement campaign and the impact of clutter on the backscattering measurements was performed to ensure the effectiveness of the calibration process (Mas et al., 2024).

The series of radar acquisitions were complemented by ancillary data, including:

- Meteorological variables, recorded every 30 min for the first two months of the campaign and every 10 min from the beginning of May. These include air humidity, precipitation, air temperature, barometric pressure, solar irradiation, and wind speed and direction.
- Soil roughness. It was characterised only once at the beginning of the growing season. It must be clarified that once plants grow the effect of soil roughness on the total radar response is expected to be much smaller than the vegetation backscatter.

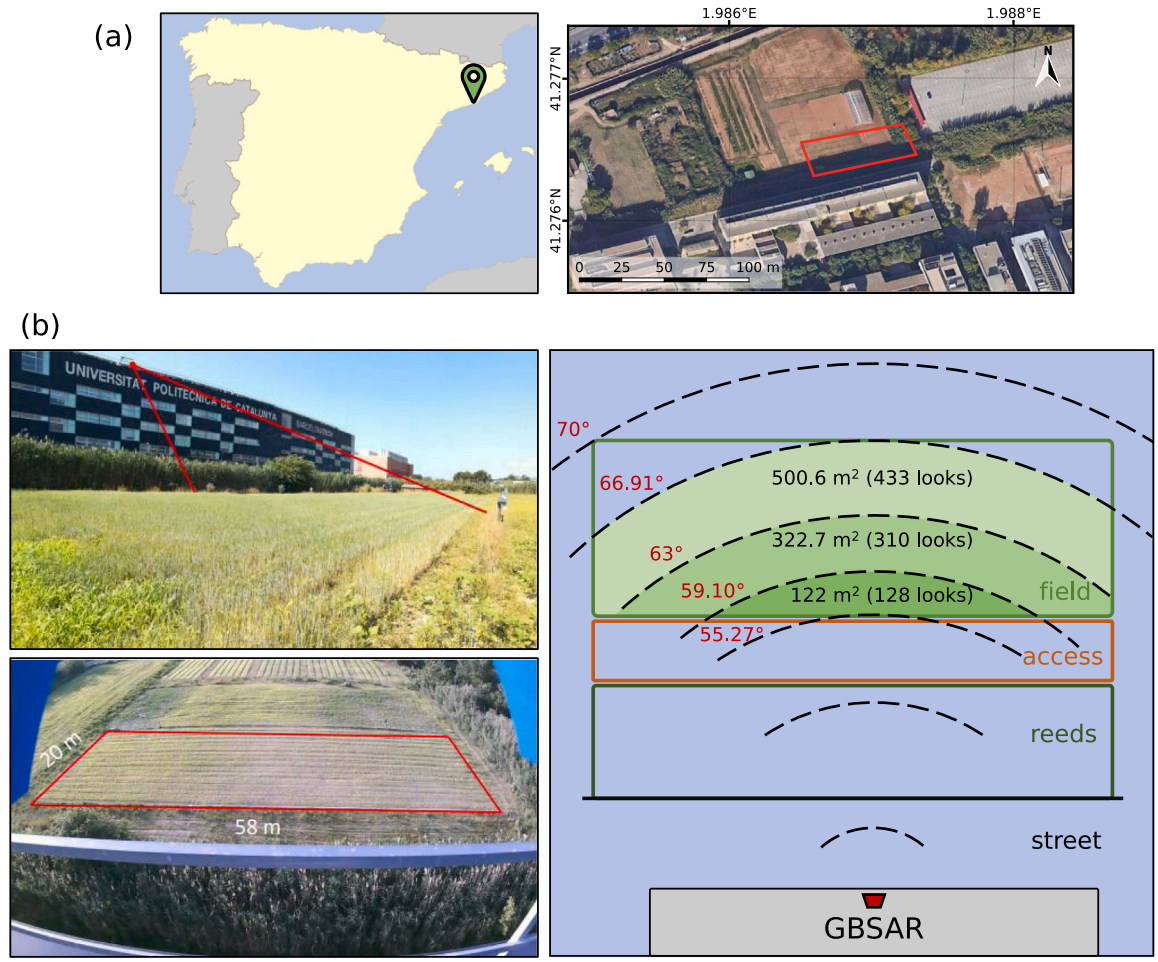

Fig. 1. (a) Test site location for the HydroSoil 2020 campaign, and placement of the field. (b) Photographs and diagram of the experimental setup. The location of the radar system on top of the building is shown on the top left. The bottom left shows the field from the perspective of the instrument. The diagram on the right shows the geometry of the experiment and the range of incidence angles. The three highlighted zones correspond to near-range, medium-range and far-range, respectively.
Source: Photographs extracted from Aguasca et al. (2020).

- Soil moisture data, acquired by various types of electronic probes. During the barley campaign, a pair of ECH2O EC-5 sensors at a depth of 15 cm were used. In the case of corn, two types of probes were used: one at a depth of 10–15 cm (HydraProbe®) and a profile probe (GroPoint®) with 3 segments measuring at different depths. Additionally, gravimetric measurements were performed every week from the beginning of May until the end of the campaign.
- Vegetation variables: plant density, planting row direction, biomass, crop phenology, leaf area index (LAI), plant height, and vegetation water content.

The campaign spanned the complete growing cycles of two different crops: barley and corn. The scope of the analysis shown in this work is limited to the first season, corresponding to barley, i.e. from mid-March until early-June. By focusing only on the barley growing season the aim was facilitating the development of a suitable methodology for the analysis of the data and to present results under the conditions of such a part of the campaign. Given the complexity and size of the dataset, this decision enabled to go in depth in multiple aspects, instead of replicating the methodology on a second crop which also presents additional features to be taken into account (e.g. irrigation, different crop type, etc.). In addition, a single manuscript including both seasons would be excessively long.

For illustration purposes, Fig. 2 shows the time series of backscattering coefficient, wind speed, SM, precipitation, plant height, and LAI for the whole barley campaign. There were 350 mm of accumulated rainfall during this period, with temperatures ranging from 3–21 °C in March, to 13–25 °C in June. The field was not irrigated during this period.

SAR data were acquired continuously from right after sowing (March 4th) until one week before harvest (June 12th), except for two non-programmed halts in April 1st and 29th. On March 14th, the COVID-19 State of Alarm was declared in Spain, entailing strict mobility restrictions that were eased starting from May 5th. As a result, field measurements started on May 7th. In May 13th it was observed that the crop was infected by *Puccinia hordei*. It is also worth noting that the maximum measured plant height at the time of grain development was approximately 40 cm, which is below the average height typically observed for spring barley. Likewise, LAI values are much lower than what would be expected for a mature barley field. Several factors contribute to this: low sowing density (Fig. 3), low plant height, the effect of waterlogging (discussed later) and the mentioned appearance of *Puccinia hordei*

2.2. Methodology

The analysis of the radar data used is specifically focused on the repeat-pass interferometric coherence. SLC images were focused following the procedure described in (Aguasca et al., 2020). Due to the viewing geometry, three different areas (near-range, medium-range,

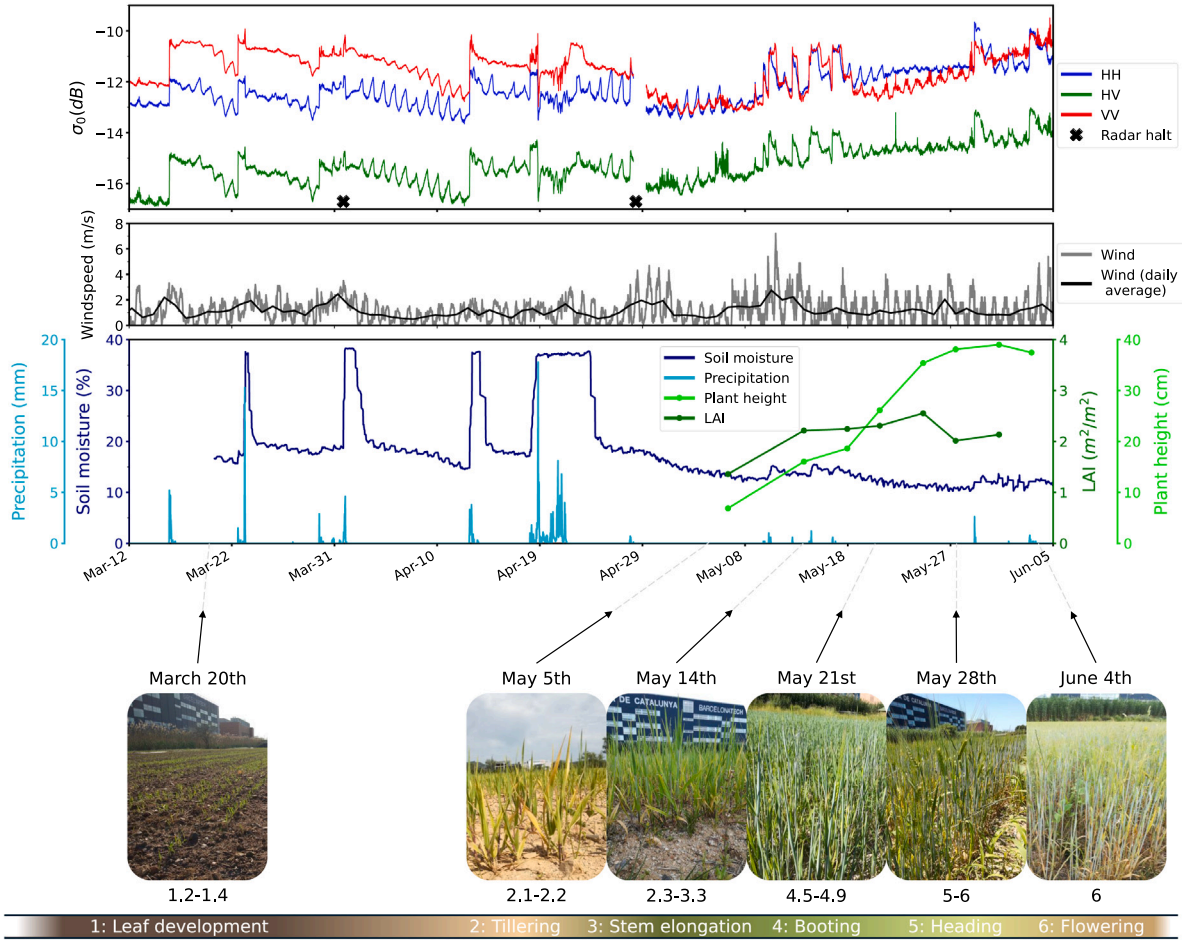

Fig. 2. From top to bottom: Backscattering time series during the barley campaign, wind speed time series, the evolution of other meteorological and ancillary parameters during this period, and an approximate calendar of the growth stages (Zadoks scale) based on in situ acquired photographs. The discontinuities in the backscatter curves correspond to halts in the acquisitions.

and far-range), as illustrated in Fig. 1b, were defined to analyse the influence of the incidence angle.

From the set of focused SLC images, multiple time series of repeat-pass coherence were constructed, differing in the way the interferograms were computed (Fig. 4):

1. Long-term (seasonal) series (e.g., Figs. 4 and 6):
   - They span the entire season, with an interferogram every 10 min.
   - Primary image changes for every interferogram.
   - A specific temporal baseline is used for each of the series built in this way: 10 and 30 min, 1, 3, 6, 12 and 18 h, and 1, 3, 6, and 12 days.
2. Short-term series (e.g., Figs. 4 and 9):
   - Four different time series for each date of the season.
   - Primary image fixed at 0:00, 6:00, 12:00 or 18:00 of the specific date.
   - The temporal baseline increases from 10 min to 12 days in 10-min steps.
3. Daily-reset series (e.g., Figs. 4 and 11):
   - Four series covering the entire season, with an interferogram every 10 min.
   - For each of the series the primary image resets daily at a specific time: 0:00, 6:00, 12:00, and 18:00.
   - The temporal baseline increases in 10-min steps from the starting time until the primary image changes again.

In summary, for the first set of series the interferograms are created with a "moving window" with a fixed width (temporal baseline) in each case. In the second set, the window moved once a day with the width progressively increasing. In the final case, the start of the window was fixed in time while the width gradually increased.

The construction of these different time series aims to highlight the sources of both short and long-term temporal decorrelation. Changes in soil properties (SM and permittivity), wind, temperature, and vegetation water content dynamics have been considered as the main sources of the short-term decorrelation. Additional decorrelation sources may explain the long term evolution of coherence, which can be classified in three groups: (1) progressive changes in vegetation, such as the evolution of its phenological stage, plant density, or biomass; (2) changes experienced by the crop that are unrelated to its growth (e.g., waterlogging, wind-induced breaking of stems or leaves, lodging, and pest infestations like *Puccinia hordei*); and (3) man-made changes in the scene caused by tasks related to field management and data acquisition.

The first point of interest has been to study the rate of decorrelation during different stages of the campaign and for different ranges of temporal baselines. Two simple functions (Morishita and Hanssen, 2015) have initially been used to describe the temporal decorrelation:

$$\gamma(t) = \gamma_0 e^{-t/\tau} \quad (1)$$

Fig. 3. Photographs showing the row orientation and the density of the crop at different stages. From top to bottom: sowing of the field on March 4th, early stage of growth (March 20th) and advanced growth stage (May 28th).
Source: Photographs extracted from Aguasca et al. (2020).

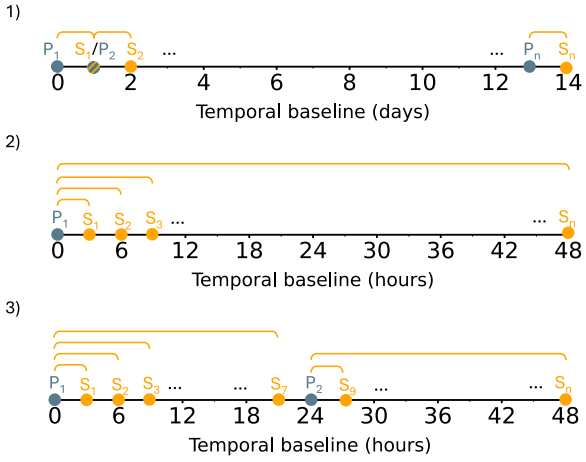

Fig. 4. From top to bottom: (1) long-term series, (2) short-term series, and (3) daily-reset series. P_i represent different primary images, while S_i denote different secondary images.

$$\gamma(t) = (\gamma_0 - \gamma_\infty)e^{-t/\tau} + \gamma_\infty \tag{2}$$

where γ_0 is the initial coherence amplitude, which should be close to 1; γ_∞ is the long-term coherence, corresponding to the minimum attainable value that the observed coherence will converge to over time; and τ represents the decorrelation rate, which is the time for the coherence to drop to $1/e$ of its initial value.

Subsequently, a new periodic term was added to Eq. (2) in order to take into account the oscillations observed in the coherence time series for sub-daily temporal baselines:

$$\gamma(t) = (\gamma_0 - \gamma_\infty)e^{-t/\tau} + A\cos\left(\frac{2\pi}{T}t + \phi_0\right) + \gamma_\infty \tag{3}$$

where ϕ_0 represents the initial phase of this oscillation; T denotes the period, associated with the daily cycles originating these fluctuations, and thus set to 1 day; and A represents the amplitude of the oscillation. This amplitude is assumed to be constant in the short term or to be attenuated over time by another decaying exponential with a new parameter τ_2: $A = A_0 e^{-t/\tau_2}$. It is important to note that Eq. (3) is defined in such a way that $\gamma(t)$ is not necessarily bound to the interval [0,1]. This is a conscious decision to avoid mixing the amplitudes of the two main terms (exponential decay and oscillating), as it enables a direct physical interpretation of the coherence as a combination of terms. In practice, as the data are never over 1, fitting the model as defined in Eq. (3) rarely produces values above 1. Consequently, despite not being mathematically bounded, such an expression is practical for interpretation and advantageous for numerical fitting. Hereafter, these three models will be referred to as "EXP" (exponential, Eq. (1)), "EXP-LONG" (exponential with a long-term coherence term, Eq. (2)), and "EXP-OSC" (the combination of an exponential decrease with a periodic oscillation, Eq. (3)), respectively.

In an effort to assess the effect of SM in the coherence time series, the in-situ SM data have been used to compute values of simulated coherence. The model proposed by Hallikainen et al. (1985) to estimate the dielectric constant of the soil surface based on SM data was employed. Then, the model described by De Zan et al. (2014) was used to derive the complex interferometric coherence from changes in the dielectric constant. The coherence magnitude obtained through this method has been compared to the coherence time series resulting from the measured data. Recall that the SM values acquired by the probes were measured for a segment between 10 and 15 cm deep. Therefore, they do not accurately reflect the SM values at the first few centimetres of soil that the microwave signal can penetrate. The estimation of surface soil moisture (SSM) from root zone data (and vice versa, which would normally be the case for the purpose of crop monitoring) is a challenging problem still under research (Wagner et al., 1999b; Cho et al., 2015; Koyama et al., 2017; Carranza et al., 2021). The impact upon the simulated coherences of the discrepancy between the depth of the SM probes and the surface SM values is discussed in Section 3.3.

While (root zone) soil moisture provides an indication of moisture availability, the vapour pressure deficit (VPD) has been used to provide an indication of atmospheric demand and potential stress. VPD drives the flow of moisture in the soil–plant–atmosphere continuum, and its daily cycle provides an indication of the timing of water flow. VPD is the difference between the amount of moisture actually present in the air and the moisture that the air, at that particular temperature, could hold at saturation. It is calculated as follows:

$$VPD = e_s \cdot \left(\frac{R_h}{100}\right) = 6.112\exp\left(\frac{17.67T}{T+243.5}\right)\cdot\left(\frac{R_h}{100}\right) \tag{4}$$

where R_h is the relative humidity, and e_s is the saturation vapour pressure at the evaporating surface, which can be expressed as a function of the temperature T (°C).

Higher values indicate faster water loss from plants due to the greater difference in water vapour pressure between the leaf and the surrounding air. In these circumstances, plants can respond by closing the stomata in the leaves to reduce ET, although this response can be influenced by climate, plant species and photosynthesis strategy (Massmann et al., 2019). Prolonged periods of high VPD values can be a sign of water stress in vegetation. Conversely, when VPD is very low, the air approaches saturation, which may result in condensation in form of dew on the plant surface. The daily cycle of VPD is included here to indicate the period during which water is being transported to the

atmosphere, and during which changes may be occurring in the amount and distribution of water within the vegetation.

As for vegetation water content (VWC), sub-daily VWC measurements are logistically challenging, labour-intensive, and time-consuming to collect using destructive sampling, especially at sub-daily scales. Sub-daily VWC could be estimated from continuous sap flow observations and estimated transpiration (Vermunt et al., 2022)). However, the required data were not collected as part of the HydroSoil campaign. Likewise, ET values could not be directly calculated. Given these limitations, and the fact that the VPD is related to the rate of ET (Rogers and Yau, 1989; Penman, 1948), VPD was used as an indicator of the sub-daily dynamics of vegetation.

3. Results

3.1. Time series of coherence amplitude with multi-day temporal baselines

The construction of time series of coherence amplitude using multiples of a day as temporal baselines allows for an analysis of the data on temporal scales comparable to SAR satellite revisit times. Fig. 5 shows multiple time series spanning the whole season corresponding to the coherence at the HH channel, obtained by setting the temporal baseline to 1, 6, and 12 days. In this case, the coherence values are estimated by averaging all the pixels within the near-range area (i.e. considering incidence angles under 59°, as shown in Fig. 1b). The time shift between the different curves is caused by the fact that the date chosen to represent each point corresponds to the date of acquisition of the secondary image. The interruption in all curves during April 29th corresponds to one of the non-programmed radar halts (Fig. 2), and it reappears 1, 6 or 12 days forward into the time series, when those acquisitions are used as primary images in the interferogram.

The 6 and 12-day baselines have been chosen to resemble the temporal baselines provided by Sentinel-1. Overall, as expected, the longer the temporal baseline, the lower the coherence. The 1-day coherence is always greater than the other two.

It is important to note that a time series of 6-day coherence of Sentinel-1 over the same site would have provided only about 14 values along the same time span (see asterisk symbols in the bottom of Fig. 5), and all of them acquired at the same time during the day. Therefore, all the fine details present in the time series shown in Fig. 5 cannot be captured by current satellite systems. In particular, with Sentinel-1, or with any conventional Low Earth Orbit satellite, one cannot sense the daily cycle of hydrometeorological variables, or the daily water cycle (how or when water goes up from soil to plants and then down to soil again), or the water stress suffered by the plants due to high temperatures during the day, etc. This motivates the proposal of new sensors with shorter (i.e., sub-daily) revisit times.

In all three curves there is an overall downwards trend as the season advances, since the increasing presence of vegetation becomes the main source of temporal decorrelation in the scene. Before April 19th, coherence is rather stable for all temporal baselines, only affected by the rain events. With 1-day baseline the values are above 0.9, whereas with 6- and 12-day baselines coherence values are around 0.8. However, later in the season the 1-day coherence progressively decays down to 0.6 at the end of the season, and the 6- and 12-day coherences are more severely affected by the presence of vegetation and reach values around 0.3 at the end of the season. Along all the season, the sudden drops in coherence correspond to rain events. The clearest example is the sharp decrease during the second half of April, caused by an intense rain period (190 mm of cumulated rainfall) from the 19th to the 22nd of April. Using different temporal baselines in remote sensing serves to focus the sensitivity of the system on specific aspects which depend on the temporal scale of their variation. For instance, the effect of rain is avoided earlier using shorter baselines, whereas the presence of vegetation growth can be monitored with longer baselines. Moreover, barley is known to be more susceptible to waterlogging (visually observed in the field on April 19th) than other crops (Setter and Waters, 2003; Xu et al., 2022). An increase in the temporal baseline in this case means that the effect of these events is registered by more interferograms (around the April 25–28th for the 6-day baseline and during the first days of May for the 12-day one). Finally, a daily ripple is observed, as the coherence is highest when the primary and secondary acquisitions are both made at night time. This will be further discussed later.

The overall evolution in the time series is observed in all the polarimetric channels. Fig. 6 again shows HH for a 1-day temporal baseline, along with HV and VV. All channels exhibit a decrease in coherence as the season advances, and they are sensitive to the rain events in March 16th and 23rd, and April 1st, 13th, 19th and 21st. Initially the cross-polar channel shows the lowest coherence values, whereas VV is the least decorrelated. However, this changes after mid May just prior to the harvest date. As seen in the backscatter curves shown in Fig. 2, for the first two months there is a stronger signal return for VV than for HH. Starting from late April, this difference shrinks, and even reverses during the second half of May. This may be due to a two-fold effect of the vertical plant stems in the field: the vertical polarisation is strongly attenuated by the vertical stems when the waves go through the vegetation volume and, simultaneously, the double bounce mechanism is more present as the crop matures, for which a double Brewster angle effect (at the stems and at the ground) results in lower response in VV (Lopez-Sanchez et al., 1999; Thirion-Lefevre and Guinvarc'h, 2018). It must be clarified that in erectophile cereals (like wheat, barley, oat, etc.), with a clearly marked vertical structure, it has been found (for instance with Sentinel-1 data) that the backscatter response at the VV channel shows a decrease when plants grow. For instance, in (Palmisano et al., 2021) we see how the VH/VV backscatter ratio increases for wheat and barley with vegetation growth despite the backscatter at VH channel is rather constant, i.e. it is due to an increased attenuation (and reduced backscatter) at the VV channel. This attenuation is also studied in a dedicated in-depth work by Arias et al. (2022). Consequently, this feature of the VV channel as a function of plant growth does not necessarily entail an increase in volume scattering (with an associated increase temporal decorrelation at the VH channel). In this case (Fig. 6), a marked decrease in γ_{VV} is observed coinciding with the period where the backscatter at HH channel (σ_{0HH}) is higher than at the VV channel (σ_{0VV}) (Fig. 2).

Fig. 7 shows once again the coherence time series obtained with a 1-day temporal baseline and a moving primary image, but this time for near, medium and far-range at each channel. The main trend, commonly observed across all channels, is a decrease in coherence as the incidence angle increases, with VV showing the highest correlations in the early months of the season, and HV the lowest. VV experiences comparably higher loss of correlation later in the season, as was previously seen in Fig. 6, as well as a bigger spread in coherence values depending on the incidence angle during the second half of May. This influence of the incidence angle over the VV coherence, with less coherence in the far range, suggests that the previously mentioned influence of attenuation and double bounce mechanism is confirmed, since shallower angles entail an increased path length within the vegetation volume and more dominance of the volume and double bounce terms compared to the surface scattering component. The volume playing an important role in the drop in coherence in VV is also consistent with Fig. 7, where the drop in coherence is largest in the far range, where one would expect limited sensitivity to the surface term.

The rain events in April 19th and 21th cause a reversal in the previously mentioned ordering, with higher coherences for the smaller (i.e. steeper) incidence angles for some days. During these days the field is waterlogged, and most of the radar signal is specularly reflected off the water surface. As a result, the backscattered intensity during these days is much lower (Fig. 2), especially for steeper incidence angles. In these conditions, SNR takes lower values for steeper angles, and its

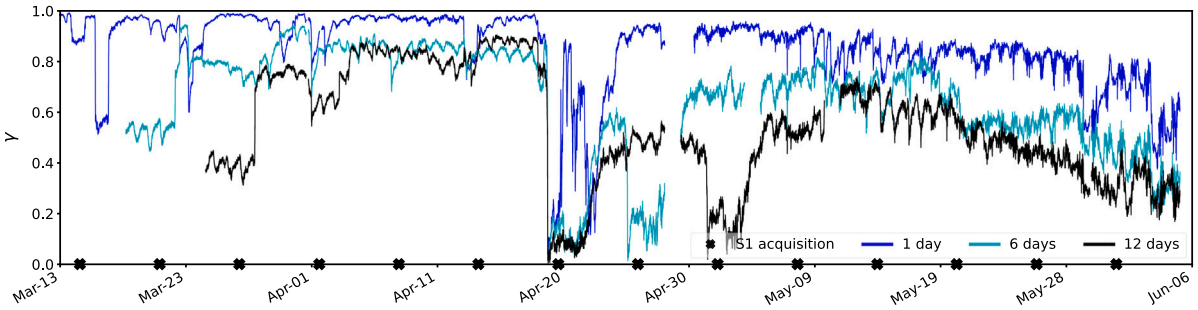

Fig. 5. Coherence time series (HH channel) for the barley season obtained with different temporal baselines: 1 day, 6 days, and 12 days. The morning acquisition times for the Sentinel-1 images covering the campaign's time frame are also shown. The x-axis corresponds to the date of the secondary image.

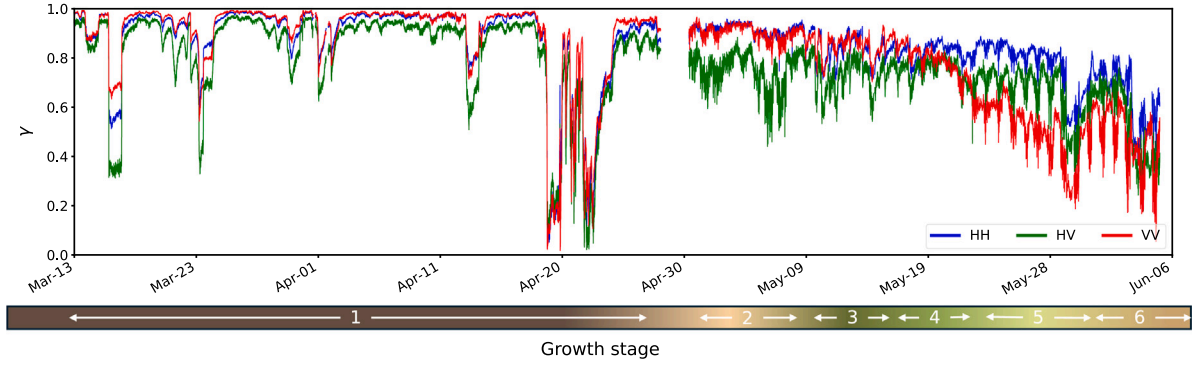

Fig. 6. Coherence time series (1-day temporal baseline) for the whole barley season at the three polarimetric channels. The x-axis corresponds to the date of the secondary image and displays the growth stage calendar.

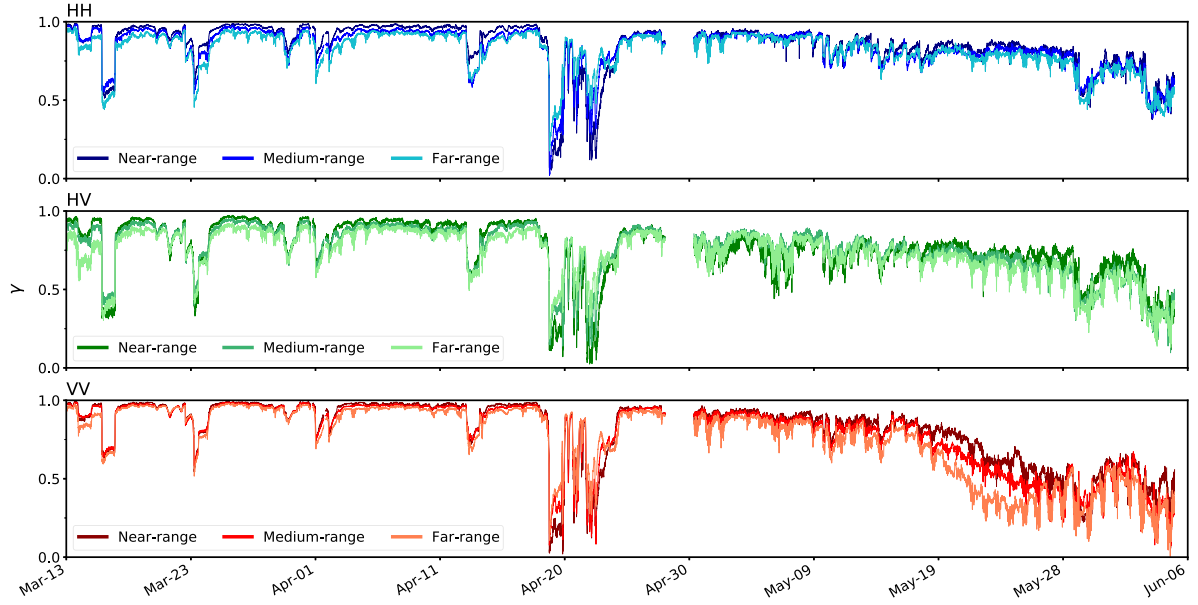

Fig. 7. Coherence time series (1-day temporal baseline) for the three channels. The different curves display the coherences estimated for different incidence angles (i.e. over the three differentiated regions shown in Fig. 1b).

contribution in the drop in coherence becomes noticeable (Zebker and Villasenor, 1992).

The effect of increasing the temporal baseline on the decorrelation rate has been studied quantitatively. Fig. 8 shows the average coherence values resulting from keeping the same primary image and increasing the temporal baseline from 1 to 12 days, setting the primary in two specific dates (April 3rd and May 19th) in the early and late stages of the campaign, respectively. In this case, the coherence is estimated by averaging all the pixels within the whole field (i.e. the combination of the three areas shown in Fig. 1b). The decrease in the coherence amplitude can be described, as expected, by Eqs. (1) and (2). Clearly, the plots obtained at the early season (top row) show a slower decorrelation than at the late season (bottom row). For the EXP model, this translates into greater τ values at the early season than at the late season, being the VV case the most extreme example. It is also observed how, irrespective of the moment of the season, the long term

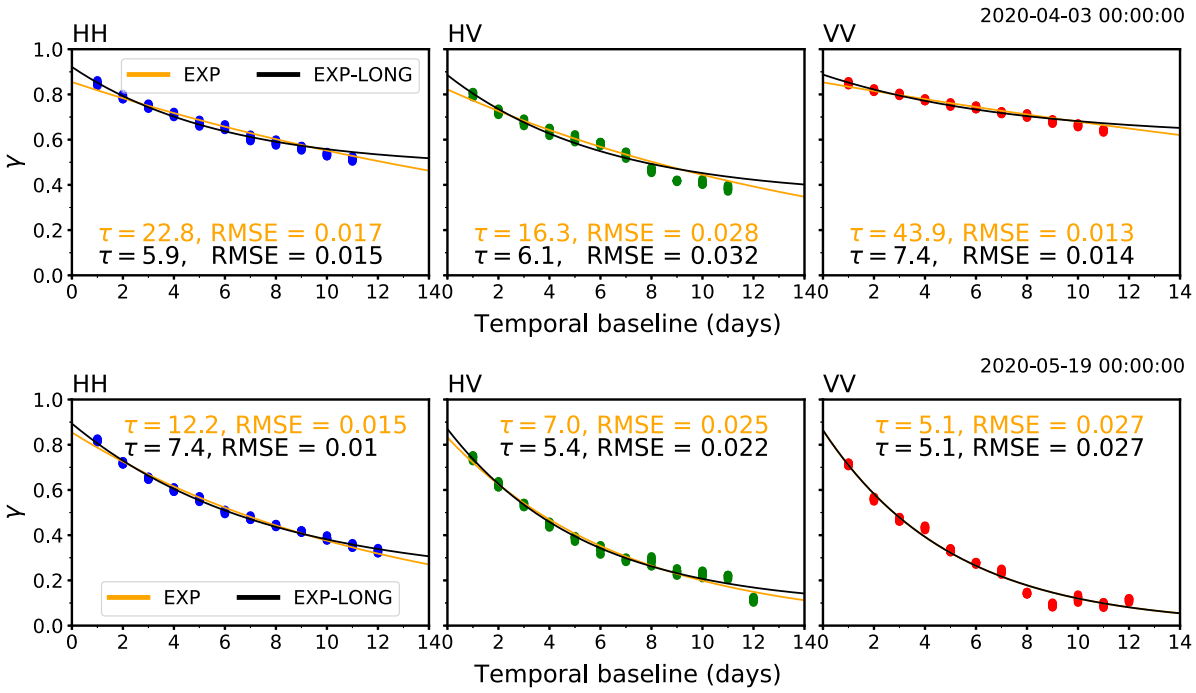

Fig. 8. Example of the decorrelation curves for the different polarimetric channels in 2 different dates: early season (top row, April 3rd) and late season (bottom row, May 19th). The primary image is set, while the temporal baseline (in days) is increased. The fitted decorrelation time (τ) and the RMSE for the fit obtained using the different models are shown.

coherence remains over 0 after 12 days. While in the early stages both co-polar channels experience a similar decline as the baseline increases, VV decorrelates similarly to HV as the season advances. These changes between early and late seasons are also observed in the values of τ obtained with the EXP-LONG model, but the differences are not as noticeable as with the EXP model.

3.2. Time series of coherence amplitude with fractional-day temporal baselines

The extension of this analysis to temporal baselines shorter than one day yields new patterns, as represented in Figs. 9 and 10. On top of the already observed progressive decay of the coherence, there is an oscillation with a period of approximately one day. This type of daily cycle, with a recovery of the coherence, has been previously observed (Monteith and Ulander, 2022; Ouaadi et al., 2024). In our case, it can be seen how this daily cycle remains recognisable for several days as the baseline keeps increasing, despite the progressive effect of the temporal decorrelation studied in the previous section.

The periodical oscillation appears well defined in the early season (Fig. 9) when the chosen primary image is acquired at nighttime or early morning. In these cases, a plateau is observed around the 1-day temporal baseline, during which the coherence remains high and approximately constant. This behaviour is not so clearly observed when the primary image is selected during daytime, especially in the evening (18:00), since the vegetation and the atmospheric conditions experiment faster changes. When this experiment is repeated later in the season (see Fig. 10), the oscillation cannot be clearly observed due to the growth of the crop.

If the long-term temporal decorrelation effects are avoided in the time series by performing a daily reset of the primary image, the resulting series of coherence are driven only by short-term changes in the scene, as illustrated by Fig. 11. The curves show the coherence amplitude from interferograms computed every 10 min with an everyday-fixed primary image (acquired at 0:00, 6:00, 12:00, or 18:00) and increasing the temporal baseline up to 1 day. In all cases the time period covered is the same. Depending on the chosen hour for the primary image, the features of the time series appear displaced along the time axis.

Typically, coherence decreases during the first part of each cycle, and it partially recovers before the reset of the primary image. It is worth highlighting how there is already some loss in coherence after the first 10 min (i.e., the first point of each time series and after the resets), most noticeably in the case of the cross-polar channel, and when the scene is less stable during the acquisition of the primary image (i.e. during the afternoon and evening). This is mainly observed at the beginning of the campaign because the backscatter from the scene is very low and, therefore, there is some decorrelation due to SNR.

The complex behaviour of the curves can be interpreted as the combination of multiple contributions:

- Coherence tends to recover after 24 h, when the observation and scene conditions at the time of acquisition of the primary and secondary images are the most similar.
- The curves show less noise and a more defined behaviour when the primary image is acquired at nighttime or early morning. Likewise, coherence can plateau or even increase at night, when the secondary image is acquired under more stable conditions (less wind, more stable temperature and SM, etc.). Fig. 12 shows this mentioned plateau during the first hours of the night, when the scene is stable. The plants absorb water until dawn, when rapid changes in water content both in soil and vegetation drive a decrease in coherence. The minimum values in these coherence oscillations appear in the middle of the day, shortly after the VPD reaches its maximum.
- An apparent recovery in the coherence is observed around 10:00–11:00 when the primary is set at 12:00 or 18:00, as seen in Figs. 9 and 11. This sort of peak in the coherence with respect to previous values is probably misleading, and actually due to the lower coherence measured before it. The scene experiences notable changes in the previous hours, which are sources of temporal decorrelation. During the first hours after sunrise there is a increase in air temperature, as well as a decrease in air humidity and SM. This phenomenon is barely noticeable for the

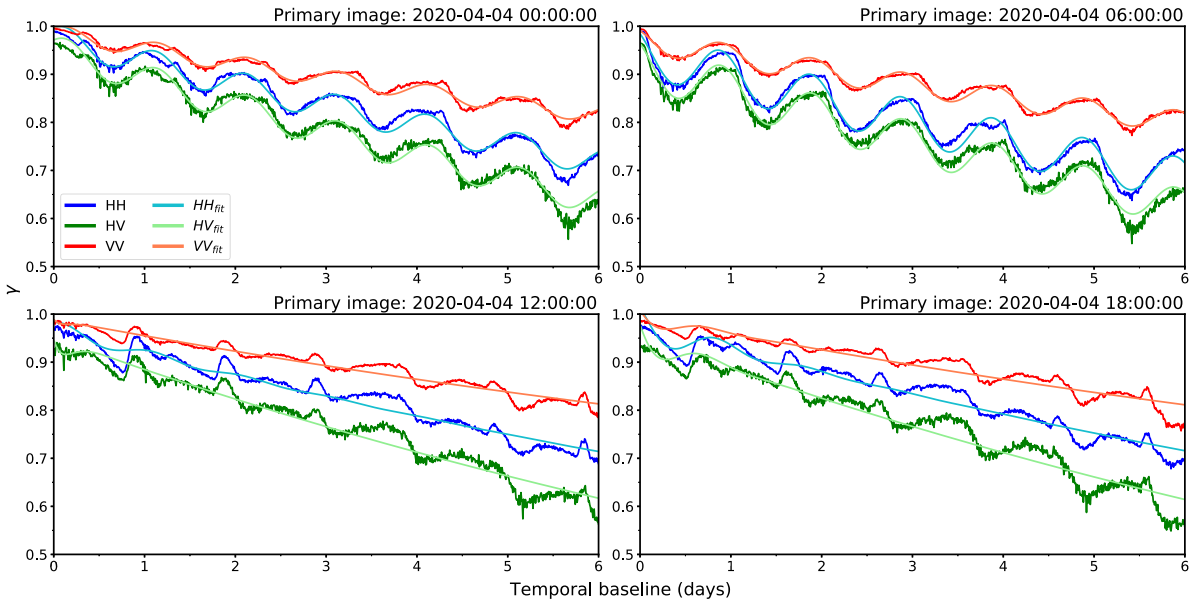

Fig. 9. Examples of the evolution of the coherence amplitude for increasing temporal baselines, from 10 min to 6 days, along with the curves obtained from the fitting parameters of the EXP-OSC model. The difference between the subplots is the acquisition time of the primary image (0:00, 6:00, 12:00 or 18:00), on April 4th.

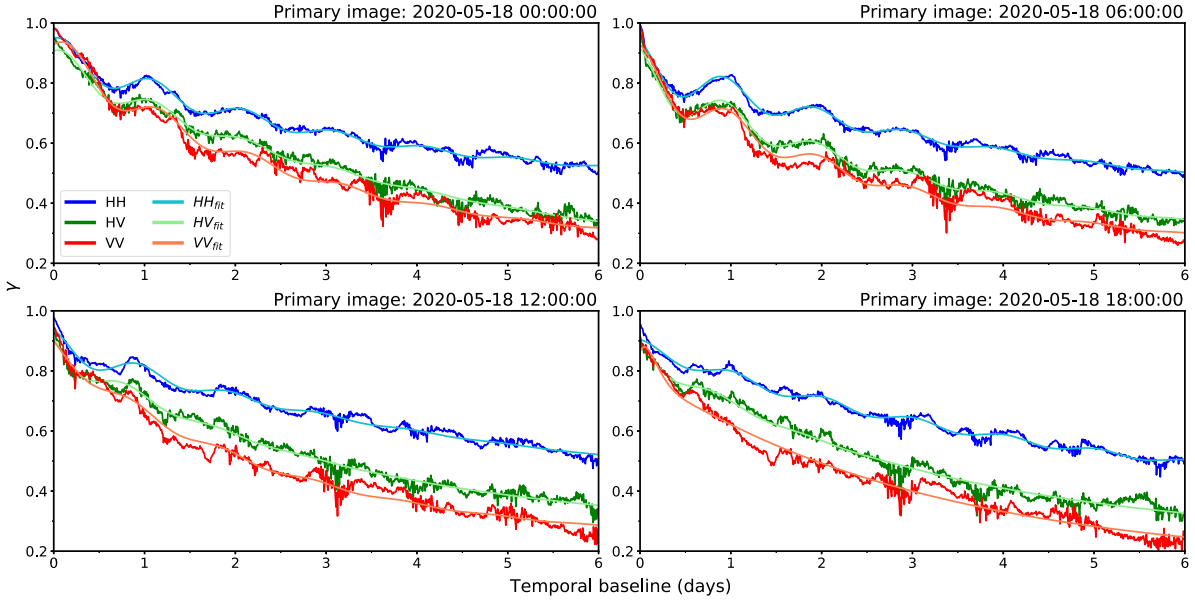

Fig. 10. Examples of the evolution of the coherence amplitude for increasing temporal baselines, from 10 min to 6 days, along with the curves obtained from the fitting parameters of the EXP-OSC model. The difference between the subplots is the acquisition time of the primary image (0:00, 6:00, 12:00 or 18:00) on May 18th.

reset at 0:00, and it cannot be seen at 6:00, but becomes more visible as the season progresses (Figs. 13–15).

- The influence of wind is variable and increases as the vegetation grows. Maximum speeds are usually recorded in the late morning or early afternoon, and while they are not reflected in these previously described coherence changes in March, they can be the main source of decorrelation later in the season. Some examples can be seen in May 10th and May 11th (Fig. 15), where some of the highest wind speeds of the campaign were recorded, around 16:00–17:00 and 9:00–10:00 respectively.
- As previously seen, VV initially experiences less temporal decorrelation than HH, but this behaviour changes by the beginning of May (Fig. 15). By that date, the presence of vegetation contributes to obscure the periodic behaviours in the curves.

3.3. Coherence time series simulated from soil moisture

The series of in situ SM data have been used to simulate the measured coherence amplitude. Fig. 16 shows the coherence time series for all polarimetric channels and for the complete growing cycle of barley, using the reset of the primary image at midnight. Given that the field did not receive irrigation during these months, and was otherwise undisturbed, the more pronounced drops in the coherence correspond to rainfall events. The dynamic range of the coherence amplitude during the day increases later in the time series, showing the increasing effect of the dynamics of the vegetation in the short-term temporal decorrelation as the plants grow.

The second and third plots in Fig. 16 display the modelled coherence and the SM data used to simulate it, respectively. The sudden increases in the SM reflect the rain events. The SM curve shows daily oscillations

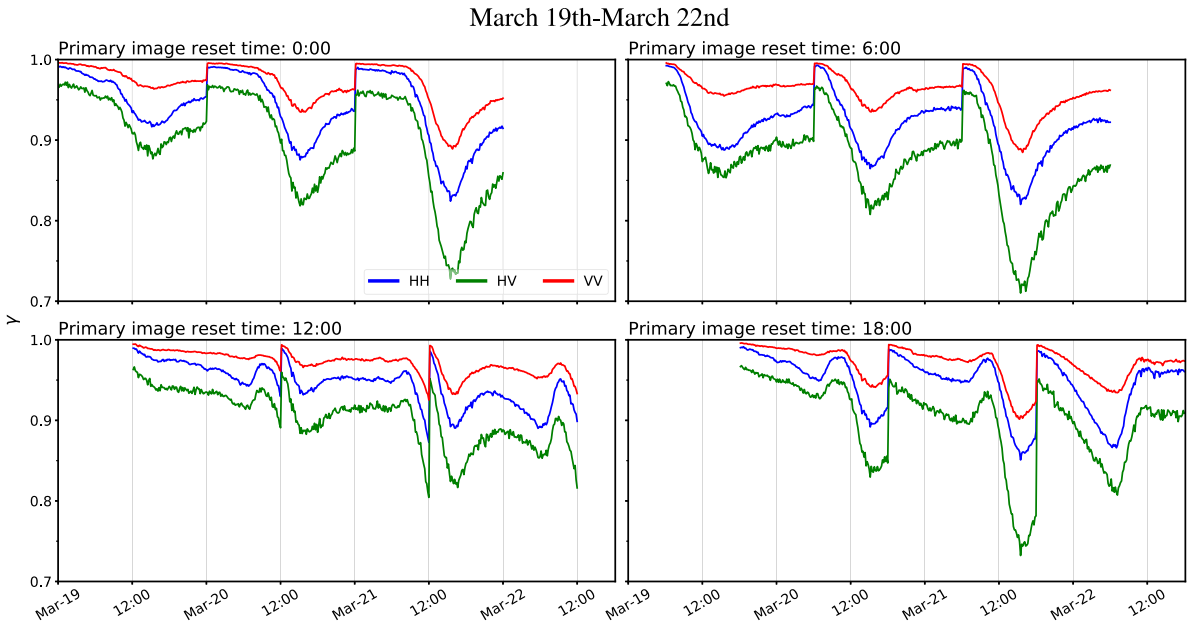

Fig. 11. Coherence time series with daily-resetting primary image. Each plot shows the result of resetting the primary image at a different moment during the day. The x-axis corresponds to the date of the secondary image.

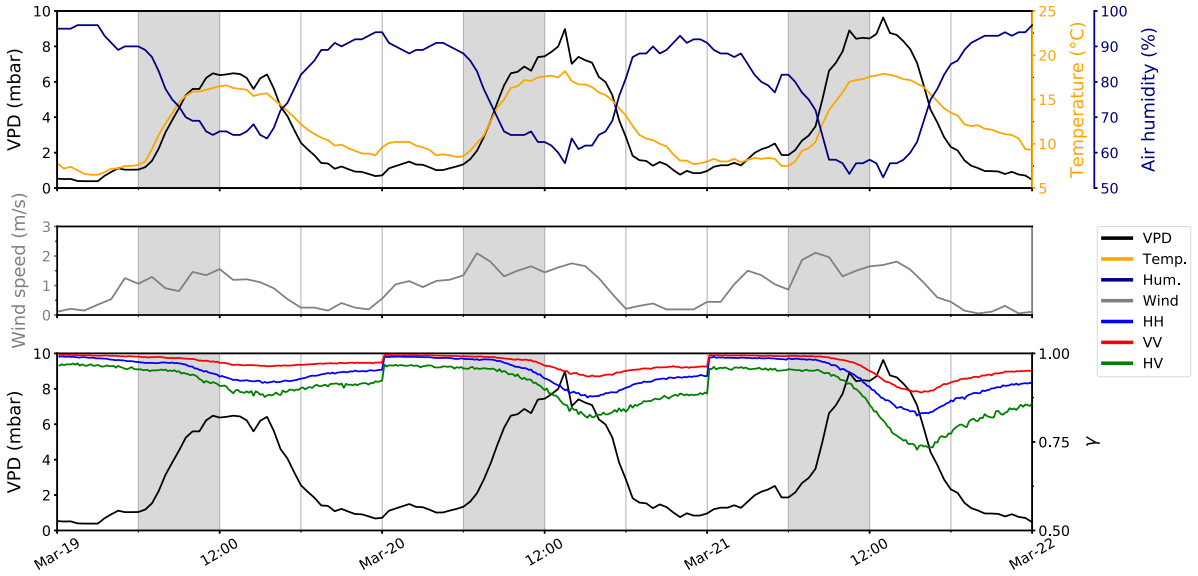

Fig. 12. Coherence time series (primary image reset at midnight) along with the time series of air humidity, temperature, VPD and wind speed over the same time period. The grey bars highlight the morning period.

and a rapid drydown after each period of rainfall. The simulated coherence captures these oscillations and shows sharp drops matching the increase, and later decrease, of SM associated with rain events.

Although the measured and the simulated coherence share the timing of the pronounced peaks, the dynamic range of the daily oscillations is considerably smaller in the simulated coherence than in the measured one. In principle, this means that the daily fluctuation in coherence cannot be solely attributed to the decorrelation caused by changes in SM. This is especially clear in the last month of the season, where the amplitude of the oscillations evidences the influence of the vegetation. However, it is also important to note that the SM data were acquired at a depth of 15 cm, while the radar is sensitive to SM in the first few centimetres of the ground. SM near the surface is highly affected by weather conditions (and irrigation if it were present). However, the dynamic range in SM values is attenuated as the depth increases (Khabbazan et al., 2022), and the influence of changes in air temperature, wind and air humidity on bare soil evaporation decreases with depth. In addition, the changes of SM at the depth of the probes (within the root zone of barley, which can reach root depths of more than 1 m, Allan et al. (1998)) are strongly influenced by the water cycle and vegetation water stress as the season progresses. In this case, the heterogeneity of the soil composition across the field could also impact how well the probes provide a representative measure of SM across the field.

According to the model (De Zan et al., 2014), a change from 0.19 to 0.18 m^3/m^3 in SM, similar to the changes found in the measured SM during one day, results in a coherence of 0.99 (Fig. 17). In order to reach the values measured (coherence around 0.95) the SM should decrease from 0.19 to 0.17, which is not what is observed in the probe measurements during the same day. This difference between modelled and observed coherence may partly be due to the difference between SSM, sensed by the C-band radar system, and the deeper SM measured

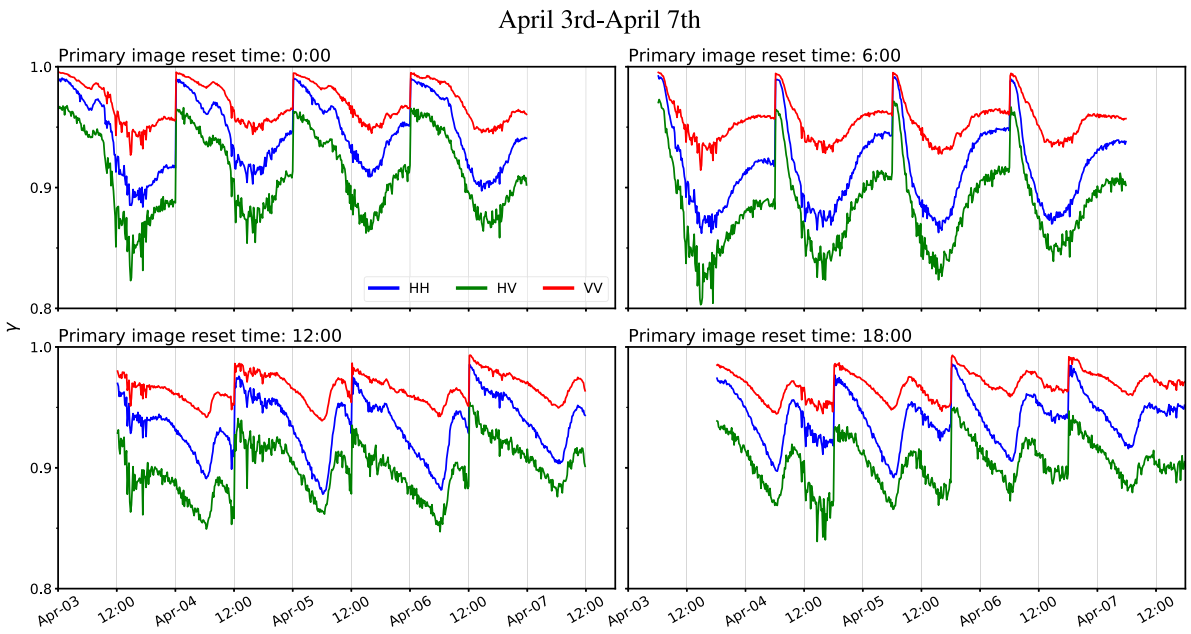

Fig. 13. Coherence time series with daily-resetting primary image for the period between April 3rd and April 7th. Each subplot shows the result of resetting the primary image at a different moment during the day. The x-axis displays the date of the secondary image.

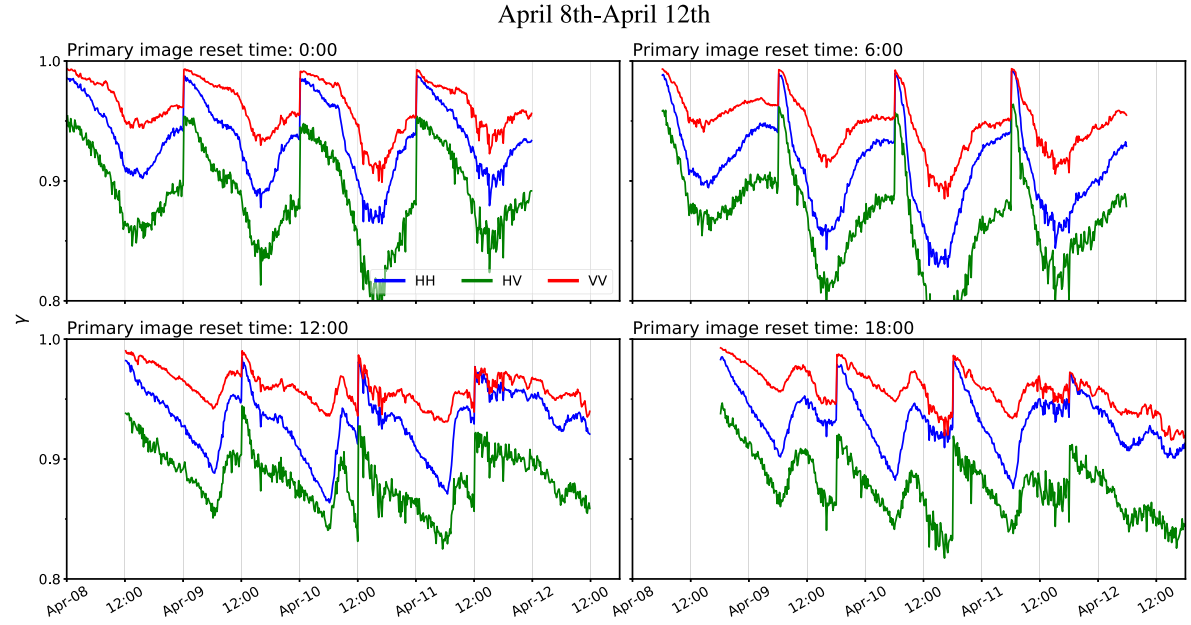

Fig. 14. Coherence time series with daily-resetting primary image for the period between April 8th and April 12th. Each subplot shows the result of resetting the primary image at a different moment during the day. The x-axis displays the date of the secondary image.

by the probe. Some initial tests were carried out in order to get a basic estimation procedure of the SSM. The assumptions were that SM changes at a certain depth would be damped compared to the surface, as seen in (Khabbazan et al., 2022), and that the dynamics of these changes would not change drastically in the first 15 cm. Based on these, linear and exponential relations between SM at the different depths were used, in order to produce new simulations of the coherence amplitude. However, they did not offer any improvement.

3.4. Daily cycle and vegetation water content

As aforementioned, to compare coherence to vegetation water dynamics, VPD time series have been calculated from temperature and relative humidity data. Fig. 18 shows again how the oscillations of VPD, air temperature and coherence are aligned along of the time series. An increase in temperature as the sun rises drives a increase in ET/water stress in the crop, and, at the same time, leads to a series of rapid changes that produce a decline in the coherence, as seen in Section 3.2. Just based on this, it is difficult to discern whether coherence is sensitive to these changes in particular. Rather, it is safe to assume that these coherence oscillations are due to a combination of the daily variations of all these hydrological and meteorological changes.

It is important to note that the oscillations in the VPD during the initial part of the season (Fig. 18, first selected period) affect a crop in its initial growth stages, while the crop's contribution to the backscattered signal is still small. Therefore, the variations in coherence must be mainly due to changes in SSM. On the other hand, the changes

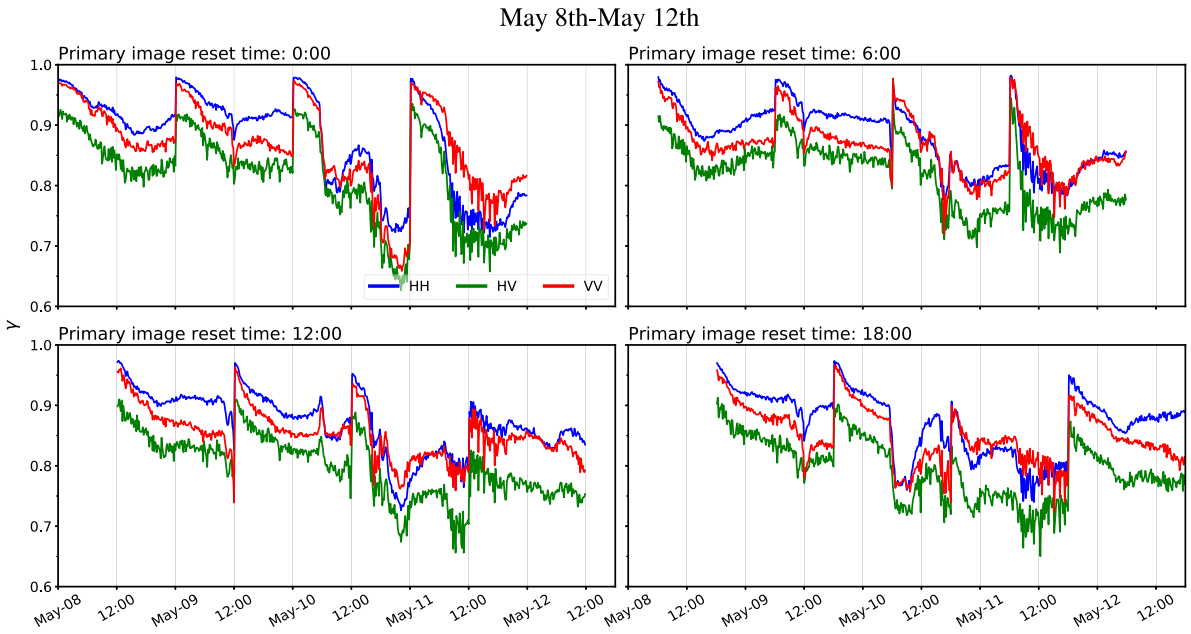

Fig. 15. Coherence time series with daily-resetting primary image for the period between May 8th and May 12th. Each subplot shows the result of resetting the primary image at a different moment during the day. The x-axis displays the date of the secondary image.

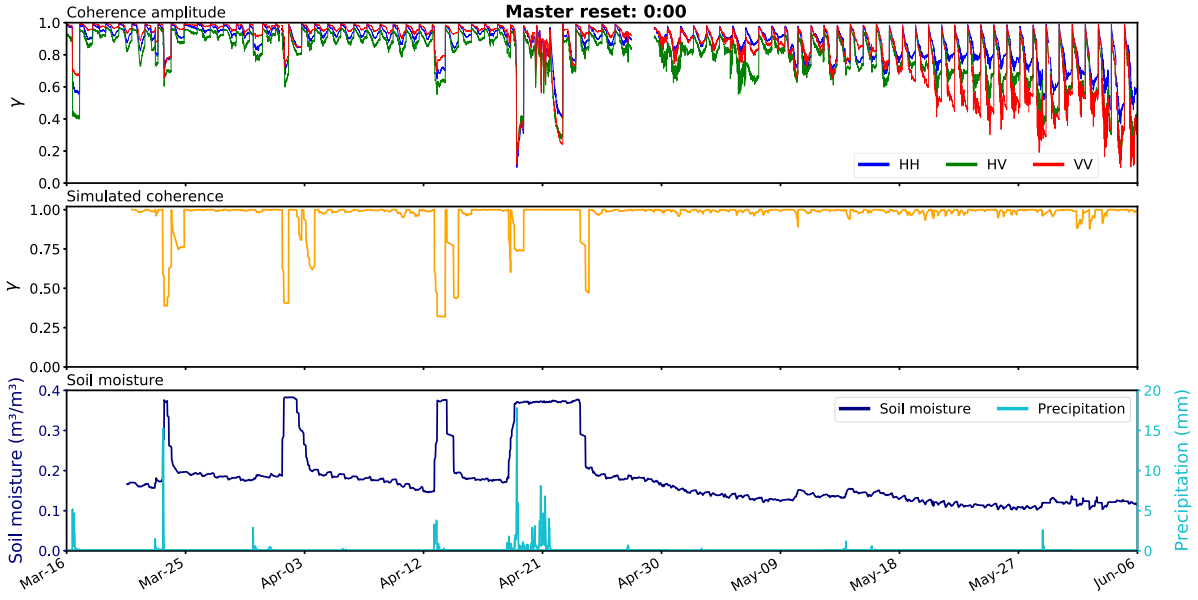

Fig. 16. Time series of coherence (daily-reset series), simulated (modelled) coherence, and soil moisture for the barley season.

in the later weeks, on top of being more pronounced, are when the crop is more mature. The increased amplitude in the oscillations of the coherence, which as seen earlier cannot be explained by SM changes, is driven by the influence of vegetation. The more irregular behaviour of the coherence series during the evening matches what had previously been observed for the evolution of the interferometric phase over tropical forests (De Zan et al., 2015), which was attributed to vegetation water dynamics. However, given that vegetation growth, vegetation movement due to wind, and changes in vegetation water content, all have an impact on the coherence, it would be difficult to directly and quantitatively relate VPD and coherence amplitude.

4. Discussion

This study constitutes an extension on previous studies that have given insights on the sub-daily dynamics of repeat-pass coherence over vegetated areas (Hamadi et al., 2014; Monteith and Ulander, 2022; Ouaadi et al., 2024).

In this work, fully-polarimetric imagery with a 10-min temporal resolution was acquired over a barley field with a ground-based C-band SAR system. This configuration allowed to have access to time series of C-band repeat-pass coherence for different polarimetric channels with a reduced temporal baseline and shallow incidence angles. A first exploratory survey was focused on studying the effect of increasing the temporal baseline, both at sub-daily and multi-day scales. As expected, shorter temporal baselines result in less temporal decorrelation, maintaining higher coherence. They also highlight the sensitivity to rain events. As in previous studies (Hamadi et al., 2014; Ouaadi et al., 2024), it has been shown how precipitation greatly affects repeat-pass coherence, and a reduced temporal baseline minimises the amount of data in the coherence time series affected by a rain event (April 20th to

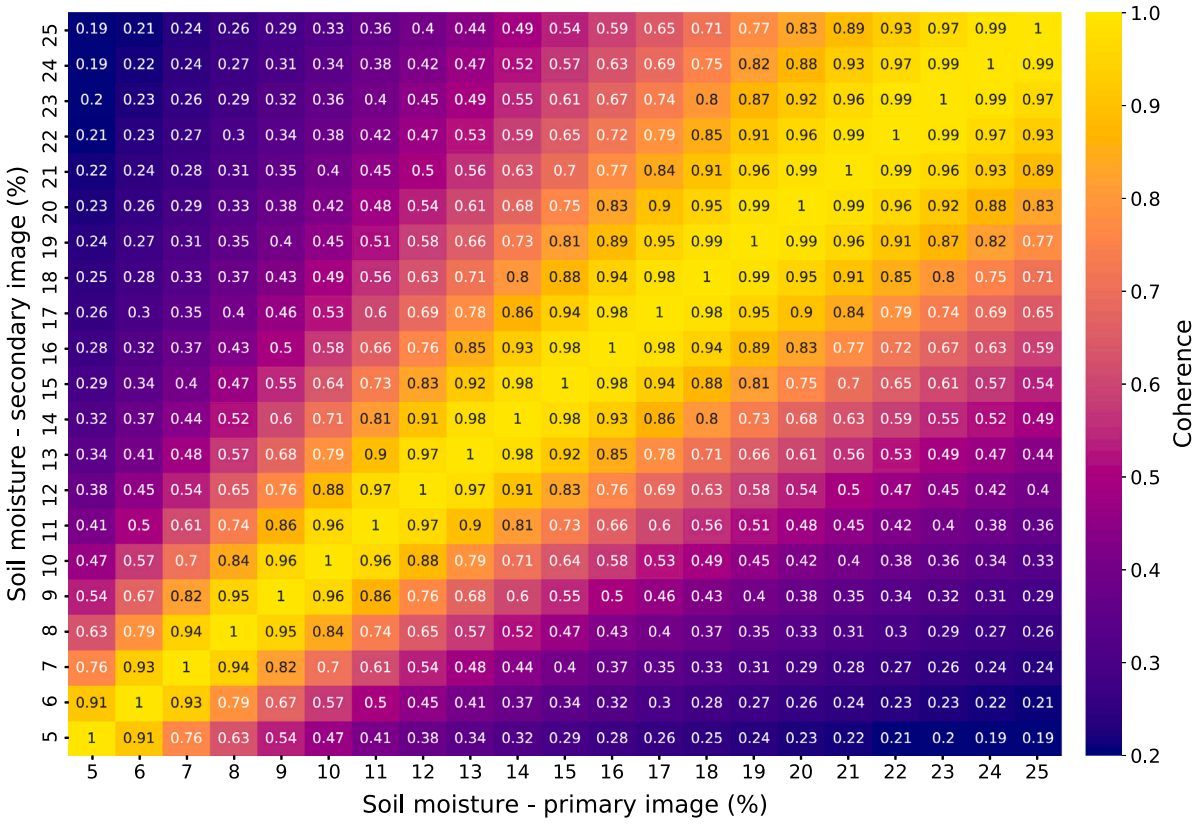

Fig. 17. Coherence for different combinations of SM values in the primary and secondary images, simulated using the models of Hallikainen et al. (1985) and De Zan et al. (2014).

May 5th, Fig. 5). This could prove valuable for sub-daily resolutions, as rain causes a decrease in sensitivity to relative changes in SM (Fig. 16) and vegetation water stress (Fig. 18).

Repeat-pass coherence already experiences a decrease for a 10-min temporal baseline, which is barely noticeable early in the season (around 0.01 for the co-polar channels and 0.03 for HV) but grows when the vegetation matures (0.03 for HH and VV, 0.09-0.1 for HV). This phenomenon has been observed for barley, which is not as dense as other crops, such as rice or wheat, due to a more open canopy structure and less foliage density (Fig. 3). Therefore, a decrease in coherence for the cross-polar channel when working with sub-daily data is expected (even for really short temporal baselines) over most crops.

The rate at which we have observed this decrease (i.e. the decorrelation rate) depends on the time of acquisition of the primary image in the interferogram, being the nighttime hours the most stable and suitable to produce a higher coherence, particularly the last few hours before dawn. Moreover, the effect of changes in the temporal baseline on the decorrelation rate has been studied quantitatively. In the case of multi-day baselines, the results are in agreement with previous observations (Ouaadi et al., 2024), where the decorrelation increases as the crop develops. In this particular case, the evolution of the coherence as the baseline increases has been modelled as a decaying exponential (Eq. (2), Fig. 8) that resembles a straight line for HH and VV when the scene is dominated by bare soil or sparse vegetation, and progressively deepens as the plants grow. The long-term coherence remains moderately high at the beginning of the season, often above 0.5 for the co-polar channels or around 0.4 for HV, and although it decreases progressively, it never reaches zero, due to the systematic bias in the coherence estimation (Touzi et al., 1999). The differences in the temporal evolution of coherence at VV in comparison to HH are worth highlighting. Both channels behave very similarly during the initial development stage of the plants, but by the end of the tillering stage VV shows increased sensitivity to the vegetation, up to the point where its decorrelation rate matches that of VH by the end of the season.

Regarding the evolution with short temporal baselines, sub-daily repeat-pass coherence (with the primary image set at midnight and baselines ranging from 15 min to one day) has previously been observed to recover by nighttime (Ouaadi et al., 2024), after decreasing during the morning and reaching its minimum relative point in the afternoon. This trend was observed throughout the season, with exception of the stage of maturity, before plant senescence. In our case, the range of temporal baselines has been increased to several days in 10 min increments, and multiple primary images were selected for different times across the day. The resulting series (Figs. 9 and 10) show this reported recovery of coherence at nighttime, but also reveal the periodicity of this pattern over multiple days, as well as some other features.

The results show how the evolution of the coherence as the baseline is increased can be modelled as the combination of an exponential decrease, that modulates the overall trend of the curve, and a daily oscillation. Therefore, the coherence amplitude tends to exhibit a partial recovery every day. In ideal conditions (a primary image acquired in a stable moment of the day and in the absence of strong sources of temporal decorrelation), one could extract the contribution of the first term of the model and be left with the periodic variations in the coherence, which resemble the daily cycle of the hydrometeorological data. The periodic oscillations are lost as the baseline keeps increasing, and they also approach noise level later in the season when the wind and vegetation changes play a larger role as sources of decorrelation. In addition, there are other characteristics of the curves that contribute to obscure this periodic pattern, as detailed in Section 3.2. In these time series (Figs. 9, 10, 11 and 13), it is again possible to see the switch in behaviour exhibited by VV (from being the least decorrelated at the beginning of the campaign to dropping to the level of HV or sometimes even lower).

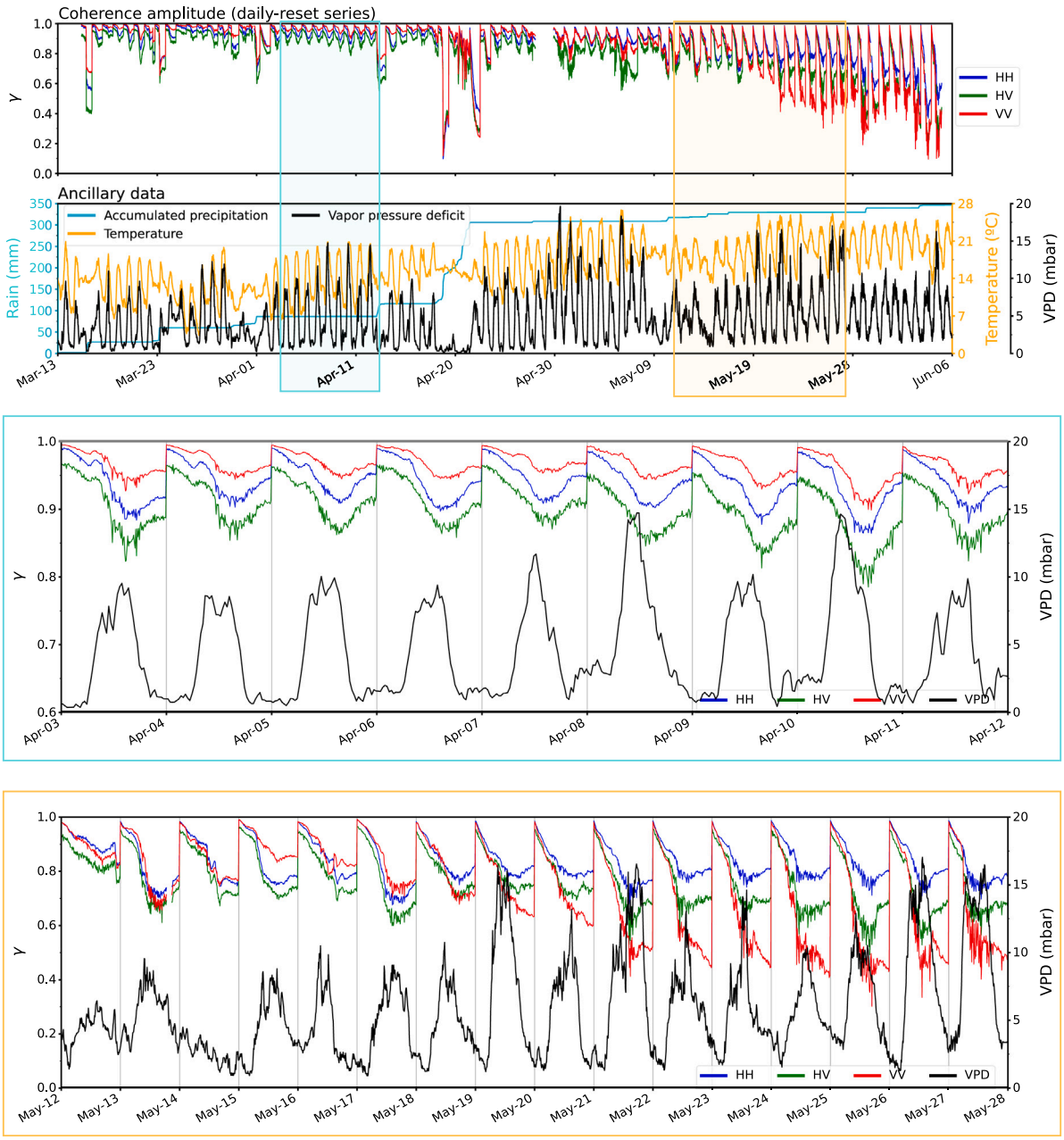

Fig. 18. Time series of coherence (daily-reset series) along with the VPD and accumulated precipitation for the barley season, as well as for two periods with little to no rain events. It should be noted that the frequency of meteorological data acquisition varied for different moments of the campaign: every 30 min in the first case, and every 10 min in the second.

The descriptive value of this model is limited, as it does not account for sudden, transient events, like precipitation, waterlogging, wind changes or other non-periodic changes in the scene. Its main value is in accounting for the periodic component that modulates coherence in this scenario (sub-daily SAR acquisitions) which is clearly correlated with the temporal pattern (sub-daily cycle) of all hydro-meteorological variables with available measures, i.e., air temperature, relative humidity, wind speed, and soil moisture. Unfortunately, all these variables are also physically coupled and intrinsically correlated in time and, consequently, we have not found a distinct link to any of them treated separately. Therefore, a proposal of a retrieval method for any of these variables based on the sole use of coherence is not possible at the moment.

Although the quantitative retrieval of hydro-meteorological variables has not been achieved, we must emphasise the potential contributions of sub-daily SAR observations to the daily water cycle. First, sub-daily SAR data are *sensitive* to the daily cycle of hydro-meteorological variables, despite not being able yet to decouple or retrieve them. Most importantly, there is room to further improvements by exploiting the whole observation space (not only coherence, i.e. including backscatter and polarimetry) which could be jointly used to tackle the separation of the various processes and the retrieval of biophysical variables.

Regarding the selection of the time of acquisition of the primary image for the interferograms, the results show how selecting a moment during the night or early morning results in higher coherences and a clearer daily pattern. Alternatively, a primary image acquired after the sunrise is very sensitive to the rapid changes that happen during the early morning (Figs. 11 and 12), resulting in a steep drop in coherence that lasts approximately until noon.

A quantitative retrieval of scene variables was not attempted in this work, but some considerations can be drawn about the optimal

measurement configurations to enhance the sensitivity to specific biophysical variables. For instance, in order to measure the progressive growth of vegetation along the cultivation cycle, it is convenient to exploit coherence measured using images acquired at night and with baselines of several days. If the focus is on the sub-daily evolution of variables, like soil moisture and vegetation water stress, then a set of measures during the day is required. From the spectrum of values found in this study, at least one measure in the night, one in the early morning, and one at noon would be required. This information, although preliminary, will be helpful in the design of the operation of future satellite missions like Hydroterra and SLAINTE.

Another objective of this work was to evaluate the impact of working with shallow incidence angles, in observation conditions comparable to those a geosynchronous SAR like Hydroterra would have over northern Europe. For these angles it was expected to see a greater influence of the vegetation. Fig. 7 shows how the greatest sensitivity to incidence angle changes is observed in VV, especially during the stages of booting and heading. The differences between channels and this increased sensitivity to particular crop stages could potentially prove useful for different applications, such as crop type mapping or crop monitoring and identification of crop phenology.

With respect to the relationship between coherence and SM, what the radar is sensitive to is the dielectric constant of the observed surface. As the dielectric constant in water changes with the temperature, this can lead to wrong assessments about SM. Due to this problem, some recent research studies opt to talk about soil permittivity (and not SM) estimation (Bhogapurapu et al., 2022; Dey et al., 2024). This same problem is seen with electronic probes, where the link between temperature and SM creates an uncertainty in the measured data. On top of this, getting accurate measurements of SSM (which C-band is sensitive to) is complicated. SM probes need to be buried at a certain depth in order to offer better results, while gravimetric measurements require samples of soil that are big enough, often requiring the extraction of soil from more than the first few centimetres. This study has not tried to find a definitive answer to the problem of linking SM at the surface and the root zone, unlike other works have (Koyama et al., 2017). SM at a depth of 15 cm was used to make a simulation of the coherence amplitude, which was found to share general trends and periodicity with the measured coherence. However, this simulated coherence could not replicate the amplitude of the daily oscillations in the coherence. In addition, this work had the chance to observe SM dynamics as regulated solely by rainfall, without scheduled irrigation, unlike the previous experience with sub-daily SAR over croplands (Ouaadi et al., 2024).

Coherence is also affected by wind, especially later in the season. However, unlike in (Ouaadi et al., 2024), a direct relationship between the minimum daily values of coherence and maximum wind speeds was not observed in all cases. Similarly, establishing a quantitative relation between VPD and coherence would be challenging due to the overlap of various sources of decorrelation. However, the timing of the VPD cycle explains the cadence of the coherence variations throughout the day, with a loss in the morning, caused by changes in SM and vegetation water content, and a re-gain during the night. This phenomenon has not been discussed much, if at all, in the literature, particularly in relation to crops.

This study opens many opportunities for future research lines. Additional analysis is recommended in order to successfully exploit coherence as a source of information about water dynamics in the scene, particularly about changes in SM and vegetation water stress. Likewise, the very frequent acquisition rate, which guarantees a high repeat-pass coherence, could allow for the use of SAR phase closure for SM retrieval. The second half of the HydroSoil campaign, during which corn was cultivated, presents different challenges and opportunities: the study of a taller and denser crop, source of a stronger temporal decorrelation late in the season; the presence of irrigation; the acquisition of rain interception data; and the possibility to explore the combination of the SM acquisitions performed through different probing methods in order to estimate of SSM. Finally, the HydroSoil facility has been recently upgraded with the capability to measure complementary parameters, such as leaf wetness and real-time wind, and to operate in dual C and X bands for evaluating the combination of multiple frequencies.

5. Conclusions

Access to sub-daily radar acquisitions has proved valuable for observing the sensitivity of SAR repeat-pass interferometry to short-term changes in soil moisture, temperature, wind or features related to daily cycles in the vegetation, which could be relevant in various scientific fields, such as hydrology and agriculture. The rate of decorrelation has been studied at different stages of the growing season of a crop, as well as the daily oscillations of the coherence for sub-daily temporal baselines, which had not been observed before. The contribution of the daily cycles of soil moisture and vegetation water dynamics in these periodic oscillations has been studied.

Additionally, the impact of changes in incidence angle and acquisition time for the primary images on the coherence time series has been assessed. The ideal time of acquisition in order to preserve a high coherence and have a clear view of the daily cycle would be nighttime and early morning, although acquisitions in the evening could benefit of the partial recovery observed at night. As for the incidence angle, it has been observed that VV is particularly sensitive to changes in phenology as the incidence angle becomes shallower. The importance of these observation conditions is relevant for the development of a geosynchronous SAR mission.

Further research should be conducted to improve the understanding of how coherence could be exploited for crop monitoring, assessment of water stress in vegetation, or for soil moisture estimation. Advances could be made in how to relate surface soil moisture (which SAR is sensitive to) to soil moisture in the root zone, where it interacts with the crop. Finally, the combination of C and X-band should be explored, as well as additional experiments to investigate coherence dynamics in other crop types. In the meantime, Hydroterra+, the successor of Hydroterra, has recently been selected as one of the four candidates to go forward with the assessment study phase for the 12th ESA's Earth Explorer mission (ESA, 2024). This underscores the urgent need to improve our understanding of coherence at sub-daily scales and develop the tools needed to exploit it for monitoring soil moisture and vegetation dynamics.

CRediT authorship contribution statement

Arturo Villarroya-Carpio: Writing – original draft, Visualization, Software, Methodology, Investigation, Formal analysis, Conceptualization. **Juan M. Lopez-Sanchez:** Writing – review & editing, Supervision, Methodology, Funding acquisition, Formal analysis, Conceptualization. **Albert Aguasca:** Writing – review & editing, Project administration, Methodology, Funding acquisition, Data curation. **Mireia Mas:** Writing – review & editing, Data curation. **Xavier Fàbregas:** Writing – review & editing, Data curation. **Antoni Broquetas:** Writing – review & editing, Funding acquisition, Data curation. **Susan C. Steele-Dunne:** Writing – review & editing, Supervision, Methodology, Formal analysis.

Declaration of competing interest

The authors declare that they have no known competing financial interests or personal relationships that could have appeared to influence the work reported in this paper.

Data availability

Data are available at the European Space Agency website in the Campaigns section.

Acknowledgements

This work was funded by the European Space Agency (ESA Contract No. 4000132509/20/NL/FF/ab with UPC), supported by the Spanish MCINN funds Unidad de Excelencia Maria de Maeztu MDM-2016-0600 and Spanish MCINN AEI under projects PID2020-117303GB-C21/AEI/10.13039/501100011033 and PID2020-117303GB-C22/AEI/10.13039/501100011033. Arturo Villarroya-Carpio enjoyed a 3-month stay at TU Delft under financial support from Banco Santander and the University of Alicante (Code: 70304B0001, Funding Line: 2023LS0048).

Susan C. Steele-Dunne was supported by the Netherlands Organisation for Scientific Research (NWO) and Netherlands Space Office (NSO) under Grant NSOKNW.2019.001.

References

Aguasca, A., Dalmau, J.B., Fabregas, X., Casamada, J.L., Mallorqui, J.J., Mas, M., Palacio, H., Broquetas, A., Gil Moya, E., 2020. HydroSoil - Ground Based SAR Experiments for Soil Moisture Measurements. Technical Report, European Space Agency, http://dx.doi.org/10.5270/ESA-ecac020.

Allan, R., Pereira, L., Raes, D., Smith, M., 1998. Crop Evapotranspiration Guidelines for Computing Crop Water Requirements FAO Irrigation and Drainage Paper 56. FAO - Food and Agriculture Organization of the United Nations., pp. 162–166, URL https://www.fao.org/4/x0490e/x0490e0e.htm.

Arias, M., Campo-Bescós, M., Arregi, LM., Gonzàlez-Audícana, M., Alvarez-Mozos, J., 2022. A new methodology for wheat attenuation correction at C-Band VV-polarized backscatter time series. IEEE Trans. Geosci. Remote Sens. 60, 1–14. http://dx.doi.org/10.1109/TGRS.2022.3176144.

Balenzano, A., Mattia, F., Satalino, G., Lovergine, F.P., Palmisano, D., Peng, J., Marzahn, P., Wegmuller, U., Cartus, O., Dabrowska-Zielinska, K., Musial, J.P., Davidson, M.W., Pauwels, V.R., Cosh, M.H., McNairn, H., Johnson, J.T., Walker, J.P., Yueh, S.H., Entekhabi, D., Kerr, Y.H., Jackson, T.J., 2021. Sentinel-1 soil moisture at 1 km resolution: a validation study. Remote Sens. Environ. 263, 112554. http://dx.doi.org/10.1016/j.rse.2021.112554.

Bamler, R., Hartl, P., 1998. Synthetic aperture radar interferometry. Inverse Problems 14, R1–54. http://dx.doi.org/10.1088/0266-5611/14/4/001.

Bauer-Marschallinger, B., Freeman, V., Cao, S., Paulik, C., Schaufler, S., Stachl, T., Modanesi, S., Massari, C., Ciabatta, L., Brocca, L., Wagner, W., 2019. Toward global soil moisture monitoring with Sentinel-1: Harnessing assets and overcoming obstacles. IEEE Trans. Geosci. Remote Sens. 57 (1), 520–539. http://dx.doi.org/10.1109/TGRS.2018.2858004.

Bhogapurapu, N., Dey, S., Bhattacharya, A., Lòpez-Martínez, C., Hajnsek, I., Rao, Y.S., 2022. Soil permittivity estimation over croplands using full and compact polarimetric SAR data. IEEE Trans. Geosci. Remote Sens. 60, 1–17. http://dx.doi.org/10.1109/TGRS.2022.3224280.

Blaes, X., Defourny, P., 2003. Retrieving crop parameters based on tandem ERS 1/2 interferometric coherence images. Remote Sens. Environ. 88 (4), 374–385. http://dx.doi.org/10.1016/j.rse.2003.08.008.

Busquier, M., Lopez-Sanchez, J.M., Mestre-Quereda, A., Navarro, E., Gonzàlez-Dugo, M.P., Mateos, L., 2020. Exploring TanDEM-X interferometric products for crop-type mapping. Remote Sens. 12 (11), http://dx.doi.org/10.3390/rs12111774.

Carranza, C., Nolet, C., Pezij, M., van der Ploeg, M., 2021. Root zone soil moisture estimation with Random Forest. J. Hydrol. 593, 125840. http://dx.doi.org/10.1016/j.jhydrol.2020.125840.

Cho, E., Choi, M., Wagner, W., 2015. An assessment of remotely sensed surface and root zone soil moisture through active and passive sensors in northeast Asia. Remote Sens. Environ. 160, 166–179. http://dx.doi.org/10.1016/j.rse.2015.01.013.

De Zan, F., Gomba, G., 2018. Vegetation and soil moisture inversion from SAR closure phases: First experiments and results. Remote Sens. Environ. 217, 562–572. http://dx.doi.org/10.1016/j.rse.2018.08.034.

De Zan, F., Parizzi, A., Prats-Iraola, P., Lòpez-Dekker, P., 2014. A SAR interferometric model for soil moisture. IEEE Trans. Geosci. Remote Sens. 52 (1), 418–425. http://dx.doi.org/10.1109/TGRS.2013.2241069.

De Zan, F., Zonno, M., Lòpez-Dekker, P., 2015. Phase inconsistencies and multiple scattering in SAR interferometry. IEEE Trans. Geosci. Remote Sens. 53 (12), 6608–6616. http://dx.doi.org/10.1109/TGRS.2015.2444431.

Dey, S., Bhogapurapu, N., Hajnsek, I., Bhattacharya, A., Siqueira, P., 2024. Soil permittivity estimation over vegetative fields using dual polarimetric SAR data. Remote Sens. Appl.: Soc. Environ. 33, 101130. http://dx.doi.org/10.1016/j.rsase.2023.101130.

Engdahl, M.E., Borgeaud, M., Rast, M., 2001. The use of ERS-1/2 tandem interferometric coherence in the estimation of agricultural crop heights. IEEE Trans. Geosci. Remote Sens. 39 (8), 1799–1806. http://dx.doi.org/10.1109/36.942558.

ESA, 2020. Report for Assessment: Earth Explorer 10 Candidate Mission Hydroterra. Technical Report, European Space Agency, Noordwijk, The Netherlands, p. 131, ESA-EOPSM-HYDRO-RP-3779.

ESA, 2024. ESA selects four new Earth Explorer mission ideas. https://www.esa.int/Applications/Observing_the_Earth/FutureEO/Preparing_for_tomorrow/ESA_selects_four_new_Earth_Explorer_mission_ideas. [Online; (Accessed 08 May 2024)].

Hallikainen, M.T., Ulaby, F.T., Dobson, M.C., El-rayes, M.A., Wu, L.k., 1985. Microwave dielectric behavior of wet soil-part 1: Empirical models and experimental observations. IEEE Trans. Geosci. Remote Sens. GE-23 (1), 25–34. http://dx.doi.org/10.1109/TGRS.1985.289497.

Hamadi, A., Albinet, C., Borderies, P., Koleck, T., Villard, L., Ho Tong Minh, D., Le Toan, T., 2014. Temporal survey of polarimetric P-Band scattering of tropical forests. IEEE Trans. Geosci. Remote Sens. 52 (8), 4539–4547. http://dx.doi.org/10.1109/TGRS.2013.2282357.

Ihuoma, S.O., Madramootoo, C.A., 2017. Recent advances in crop water stress detection. Comput. Electron. Agric. 141, 267–275. http://dx.doi.org/10.1016/j.compag.2017.07.026.

Khabbazan, S., Steele-Dunne, S., Vermunt, P., Judge, J., Vreugdenhil, M., Gao, G., 2022. The influence of surface canopy water on the relationship between L-band backscatter and biophysical variables in agricultural monitoring. Remote Sens. Environ. 268, 112789. http://dx.doi.org/10.1016/j.rse.2021.112789.

Khabbazan, S., Vermunt, P., Steele-Dunne, S., Arntz, L., Marinetti, C., Valk, D., Iannini, L., Molijn, R., Westerdijk, C., van der Sande, C., 2019. Crop monitoring using Sentinel-1 data: A case study from The Netherlands. Remote Sens. 11, 1887. http://dx.doi.org/10.3390/rs11161887.

Kornelsen, K.C., Coulibaly, P., 2013. Advances in soil moisture retrieval from synthetic aperture radar and hydrological applications. J. Hydrol. 476, 460–489. http://dx.doi.org/10.1016/j.jhydrol.2012.10.044.

Koyama, C., Liu, H., Takahashi, K., Shimada, M., Watanabe, M., Khuut, T., Sato, M., 2017. In-situ measurement of soil permittivity at various depths for the calibration and validation of low-frequency SAR soil moisture models by using GPR. Remote Sens. 9, 580. http://dx.doi.org/10.3390/rs9060580.

Le Hegarat-Mascle, S., Zribi, M., Alem, F., Weisse, A., Loumagne, C., 2002. Soil moisture estimation from ERS/SAR data: toward an operational methodology. IEEE Trans. Geosci. Remote Sens. 40 (12), 2647–2658. http://dx.doi.org/10.1109/TGRS.2002.806994.

Liu, C.a., Chen, Z., Shao, Y., Chen, J.s., Tuya, H., Pan, H., 2019. Research advances of SAR remote sensing for agriculture applications: A review. J. Integr. Agric. 18, 506–525. http://dx.doi.org/10.1016/S2095-3119(18)62016-7.

Lopez-Sanchez, J.M., Ballester-Berman, J.D., 2009. Potentials of polarimetric SAR interferometry for agriculture monitoring. Radio Sci. 44, http://dx.doi.org/10.1029/2008RS004078.

Lopez-Sanchez, J.M., Esteban, H., Baquero, M., Fortuny, J., 1999. An electromagnetic scattering model for multiple tree trunks above a tilted rough ground plane. IEEE Trans. Geosci. Remote Sens. 37 (2), 659–667. http://dx.doi.org/10.1109/36.752183.

Mandal, D., Bhattacharya, A., Rao, Y.S., 2021. Radar Remote Sensing for Crop Biophysical Parameter Estimation. Springer, http://dx.doi.org/10.1007/978-981-16-4424-5.

Mas, M., Aguasca, A., Broquetas, A., Fàbregas, X., Mallorquí, J.J., Llop, J., Lopez-Sanchez, J.M., Kubanek, J., 2024. Facility for continuous agricultural field monitoring with a GB-PolSAR. IEEE J. Sel. Top. Appl. Earth Obs. Remote Sens. 17, 11866–11876. http://dx.doi.org/10.1109/JSTARS.2024.3420392.

Massmann, A., Gentine, P., Lin, C., 2019. When does vapor pressure deficit drive or reduce evapotranspiration? J. Adv. Modelling Earth Syst. 11, http://dx.doi.org/10.1029/2019MS001790.

Mestre-Quereda, A., Lopez-Sanchez, J.M., Vicente-Guijalba, F., Jacob, A.W., Engdahl, M.E., 2020. Time-series of Sentinel-1 interferometric coherence and backscatter for crop-type mapping. IEEE J. Sel. Top. Appl. Earth Obs. Remote Sens. 13, 4070–4084. http://dx.doi.org/10.1109/JSTARS.2020.3008096.

Michaelides, R., Zebker, H., 2020. Feasibility of retrieving soil moisture from InSAR decorrelation phase and closure phase. In: IGARSS 2020 - 2020 IEEE International Geoscience and Remote Sensing Symposium. pp. 12–15. http://dx.doi.org/10.1109/IGARSS39084.2020.9323833.

Mohanty, B.P., Cosh, M.H., Lakshmi, V., Montzka, C., 2017. Soil moisture remote sensing: State-of-the-science. Vadose Zone J. 16 (1), vzj2016.10.0105. http://dx.doi.org/10.2136/vzj2016.10.0105.

Monteith, A.R., Ulander, L.M.H., 2022. A tower-based radar study of temporal coherence of a boreal forest at P-, L-, and C-bands and linear cross polarization. IEEE Trans. Geosci. Remote Sens. 60, 1–15. http://dx.doi.org/10.1109/TGRS.2021.3074098.

Morishita, Y., Hanssen, R.F., 2015. Temporal decorrelation in L-, C-, and X-band satellite radar interferometry for pasture on drained peat soils. IEEE Trans. Geosci. Remote Sens. 53 (2), 1096–1104. http://dx.doi.org/10.1109/TGRS.2014.2333814.

Morrison, K., Bennett, J.C., Nolan, M., Menon, R., 2011. Laboratory measurement of the DInSAR response to spatiotemporal variations in soil moisture. IEEE Trans. Geosci. Remote Sens. 49 (10), 3815–3823. http://dx.doi.org/10.1109/TGRS.2011.2132137.

Nasirzadehdizaji, R., Cakir, Z., Balik Sanli, F., Abdikan, S., Pepe, A., Calò, F., 2021. Sentinel-1 interferometric coherence and backscattering analysis for crop monitoring. Comput. Electron. Agric. 185, 106118. http://dx.doi.org/10.1016/j.compag.2021.106118.

Nikaein, T., Iannini, L., Molijn, R.A., Lopez-Dekker, P., 2021. On the value of Sentinel-1 InSAR coherence time-series for vegetation classification. Remote Sens. 13 (16), http://dx.doi.org/10.3390/rs13163300.

Ouaadi, N., Jarlan, L., Ezzahar, J., Khabba, S., Dantec, V.L., Rafi, Z., Zribi, M., Frison, P.L., 2020a. Water stress detection over irrigated wheat crops in semi-arid areas using the diurnal differences of Sentinel-1 backscatter. In: 2020 Mediterranean and Middle-East Geoscience and Remote Sensing Symposium (M2GARSS). IEEE, pp. 306–309. http://dx.doi.org/10.1109/M2GARSS47143.2020.9105171.

Ouaadi, N., Jarlan, L., Ezzahar, J., Zribi, M., Khabba, S., Bouras, E., Bousbih, S., Frison, P.L., 2020b. Monitoring of wheat crops using the backscattering coefficient and the interferometric coherence derived from Sentinel-1 in semi-arid areas. Remote Sens. Environ. 251, 112050. http://dx.doi.org/10.1016/j.rse.2020.112050.

Ouaadi, N., Jarlan, L., Villard, L., Chakir, A., Khabba, S., Fanise, P., Kasbani, M., Rafi, Z., Le Dantec V. Ezzahar, J., Frison, P.L., 2024. Temporal decorrelation of C-band radar data over wheat in a semi-arid area using sub-daily tower-based observations. Remote Sens. Environ. 304, 114059. http://dx.doi.org/10.1016/j.rse.2024.114059.

Palmisano, D., Mattia, F., Balenzano, A., Satalino, G., Pierdicca, N., Guarnieri, A.V.M., 2021. Sentinel-1 sensitivity to soil moisture at high incidence angle and the impact on retrieval over seasonal crops. IEEE Trans. Geosci. Remote Sens. 59 (9), 7308–7321. http://dx.doi.org/10.1109/TGRS.2020.3033887.

Palmisano, D., Satalino, G., Balenzano, A., Mattia, F., 2022. Coherent and incoherent change detection for soil moisture retrieval from Sentinel-1 data. IEEE Geosci. Remote Sens. Lett. 19, 1–5. http://dx.doi.org/10.1109/LGRS.2022.3154631.

Pandit, A., Sawant, S., Mohite, J., Pappula, S., 2022. Sentinel-1-derived coherence time-series for crop monitoring in Indian agriculture region. Geocarto Int. 1–21. http://dx.doi.org/10.1080/10106049.2021.2022008.

Penman, H., 1948. Natural evaporation from open water, bare soil and grass. Proc. R. Soc. Lond. 193, 120–145. http://dx.doi.org/10.1098/rspa.1948.0037.

Rogers, R.R., Yau, M., 1989. A Short Course in Cloud Physics, third ed. Butterworth-Heinemann, Oxford;Boston.

Sarabandi, K., Ulaby, F., Tassoudji, M., 1990. Calibration of polarimetric radar systems with good polarization isolation. IEEE Trans. Geosci. Remote Sens. 28, 70–75. http://dx.doi.org/10.1109/36.45747.

Seneviratne, S., Corti, T., Davin, E., Hirschi, M., Jaeger, E., Lehner, I., Orlowsky, B., Teuling, A., 2010. Investigating soil moisture-climate interactions in a changing climate: A review. Earth-Sci. Rev. 99, 125–161. http://dx.doi.org/10.1016/j.earscirev.2010.02.004.

Setter, T., Waters, I., 2003. Review of prospects for germplasm improvement for waterlogging tolerance in wheat, barley and oats. Plant Soil 253, 1–34. http://dx.doi.org/10.1023/A:1024573305997.

Shi, J., Wang, J., Hsu, A.Y., O'Neill, P.E., Engman, E.T., 1997. Estimation of bare surface soil moisture and surface roughness parameter using L-band SAR image data. IEEE Trans. Geosci. Remote Sens. 35 (5), 1254–1266. http://dx.doi.org/10.1109/36.628792.

Steele-Dunne, S.C., Bastos, A., Massari, C., Milodowski, D., Miralles, D., De Santis D. Tronquo, E., Ciabatta, L., Zappa, L., Dorigo, W., 2024. A SAR mission concept for sub-daily microwave remote sensing of vegetation. In: Invited Session 3D Microwave Remote Sensing of Vegetation. EUSAR.

Steele-Dunne, S.C., McNairn, H., Monsivais-Huertero, A., Judge, J., Liu, P.W., Papathanassiou, K., 2017. Radar remote sensing of agricultural canopies: A review. IEEE J. Sel. Top. Appl. Earth Obs. Remote Sens. 10 (5), 2249–2273. http://dx.doi.org/10.1109/JSTARS.2016.2639043.

Thirion-Lefevre, L., Guinvarc'h, R., 2018. The double Brewster angle effect. C. R. Phys. 19 (1), 43–53. http://dx.doi.org/10.1016/j.crhy.2018.02.003.

Touzi, R., Lopes, A., Bruniquel, J., Vachon, P., 1999. Coherence estimation for SAR imagery. IEEE Trans. Geosci. Remote Sens. 37 (1), 135–149. http://dx.doi.org/10.1109/36.739146.

van Emmerik, T., Steele-Dunne, S.C., Judge, J., van de Giesen, N., 2015. Impact of diurnal variation in vegetation water content on radar backscatter from maize during water stress. IEEE Trans. Geosci. Remote Sens. 53, 3855–3869. http://dx.doi.org/10.1109/TGRS.2014.2386142.

Vermunt, P., Steele-Dunne, S., Khabbazan, S., Judge, J., van de Giesen, N., 2022. Extrapolating continuous vegetation water content to understand sub-daily backscatter variations. Hydrol. Earth Syst. Sci. 26, 1223–1241. http://dx.doi.org/10.5194/hess-26-1223-2022.

Villarroya-Carpio, A., Lopez-Sanchez, J.M., 2023. Multi-annual evaluation of time series of Sentinel-1 interferometric coherence as a tool for crop monitoring. Sensors 23, 1833. http://dx.doi.org/10.3390/s23041833.

Villarroya-Carpio, A., Lopez-Sanchez, J.M., Engdahl, M.E., 2022. Sentinel-1 interferometric coherence as a vegetation index for agriculture. Remote Sens. Environ. 280, 113208. http://dx.doi.org/10.1016/j.rse.2022.113208.

Wagner, W., Lemoine, G., Borgeaud, M., Rott, H., 1999a. A study of vegetation cover effects on ERS scatterometer data. IEEE Trans. Geosci. Remote Sens. 37 (2), 938–948. http://dx.doi.org/10.1109/36.752212.

Wagner, W., Lemoine, G., Rott, H., 1999b. A method for estimating soil moisture from ERS scatterometer and soil data. Remote Sens. Environ. 70 (2), 191–207. http://dx.doi.org/10.1016/S0034-4257(99)00036-X.

Wegmuller, U., Werner, C., 1997. Retrieval of vegetation parameters with SAR interferometry. IEEE Trans. Geosci. Remote Sens. 35 (1), 18–24. http://dx.doi.org/10.1109/36.551930.

Xu, Z., Shen, Q., Zhang, G., 2022. The mechanisms for the difference in waterlogging tolerance among sea barley, wheat and barley. Plant Growth Regulat. 96, 431–441. http://dx.doi.org/10.1007/s10725-021-00789-3.

Zebker, H.A., Villasenor, J.D., 1992. Decorrelation in interferometric radar echoes. IEEE Trans. Geosci. Remote Sens. 30 (5), 950–959. http://dx.doi.org/10.1109/36.175330.